EarthArXiv Peer Review Statement:

This manuscript has been submitted for publication to the journal *Earth Surface Processes and Landforms*. Although this manuscript has undergone peer-review and has been accepted for publication, it has not yet been published and is undergoing final editorial checks. Subsequent versions may have minor differences. When the manuscript is published in the journal, this document will be updated with DOI link to the peer-reviewed published manuscript given by the publisher.

Planform geometric classification of fluvial and tidal channels via machine learning

Kevin K. Gardner, Rebecca J. Dorsey

Department of Earth Sciences, University of Oregon,

100 Cascade Hall, 1272 13th Avenue Eugene, OR 97403 (USA)

Emails

Kevin K. Gardner: kgardne2@uoregon.edu

Rebecca J. Dorsey: rdorsey@uoregon.edu

Keywords: tidal, fluvial, channel morphology, machine learning, geomorphology, classification

Data Availability Statement

The data that supports the findings of this study are openly available at the OpenScienceFramework repository: https://osf.io/ah46v/

Conflict of Interest Disclosure

The authors attest that they have no conflicts of interest of any kind related to this work or the publication of this research.

Funding Statement

This research was supported by the National Science Foundation grant EAR-1925560 to Dorsey

Ethics Statement

No ethics review was required; however, the authors confirm that the ethical guidelines laid forth by the publisher have been adhered to.

ABSTRACT

Despite forming under different flow conditions, the geometries of tidal and fluvial channel planforms and planform transformations display significant overlap, hindering efforts to differentiate them geometrically. Although studies have demonstrated that gobally, tidal and fluvial planforms are statistically distinct based on meander metrics, there are currently no machine-learning methodologies for classifying channels as tidal or fluvial that do not focus on meander-specific geometries. In this study we present a methodology for classifying channel planforms as tidal or fluvial using statistical representations of channel planforms and machine-learning algorithms. Using a dataset of 4294 tidal and fluvial channel segments (63 channel reaches), we trained three machine learning classifiers (Logistic Regression, Multi-layer Perceptron, and Random Forest) across 69 trials to identify the machine-learning algorithm and variables that perform best at classifying channel reaches. We evaluated the performance of the classifiers at three thresholds based on the percent of channel segments correctly identified in a given reach (>50%, >66%, and >75%). At the >50% classification threshold, all three classifiers attained a 95% reach-scale accuracy during individual trials. However, at higher classification thresholds the Random Forest classifier performed best. Feature importances from the Random Forest classifier indicate that measures of the central tendency and minimum/maximum of the normalized radius of curvature convolved with normalized width of a channel segments play a key role in differentiating between the planforms, with normalized width also contributing to the difference. This indicates that the relationship between width and radius of curvature is more important than width or measures of curvature on their own. This result likely reflects the downstream funneling of tidal channels and the limitation on the sharpness of bends associated with increased width. These methods have potential for application in the study of channels preserved on relict geomorphic surfaces and mixed-energy settings.

INTRODUCTION

Channels are ubiquitous elements of fluvial and tidal systems that span a wide range of scales, shapes, and lengths (Figure 1). Channel planforms are the 2-dimensional top-down geometry which, in the simplest form, are described using width and curvature signals along a centerline (Vermeulen et al., 2016). In fluvial settings, flow is unidirectional with variable discharge, reaching maximum discharge during floods (Leopold et al., 1964; Lutscher et al., 2007). Conversely, tidal settings are characterized by bimodal flows created by diurnal and semidiurnal flood and ebb tides

Figure 1: Examples of tidal channels and digitized planforms in: A) Ganges-Brahmaputra, Bangladesh ; B) Brussa,Italy; and fluvial channels and digitized planforms of the C) Congaree River, South Carolina, USA; and D) Latorica River, Slovakia. Note the widening of the tidal channels in the seaward direction in A and B. Digitized banks shown by the white lines. Image Credits – Google Earth V 7.3.6.10201 – A: (1/11/2023) 45Q 783344.84 m E, 2441992.03 m N. Eye altitude: 67.72. Airbus, Maxar Technologies, TerraMetrics 2024, earth.google.com [10/8/2024]; B: (2/20/2024) 33T 342377.00 m E, 5056617.19 m N, Eye Altitude: 736 m. Airbus 2024, earth.google.com [10/8/2024] C: (6/14/2024) 17S 516492.90 m E, 3742013.75 m N, Eye altitude 29.78 km. Airbus 2024, earth.google.com [10/8/2024]; D: (6/12/2020) 34U 565715.29 m E, 5373520.49 m N, Eye altitude: 8.71 km. Eurosense/Geodis Slovakia 2024, earth.google.com [10/8/2024]

where discharge is regular and reaches a maximum during fortnightly spring tides (Fagherazzi et al., 2004; Hughes, 2012; Kvale et al., 1995). Despite these differences in flow conditions, there is a significant overlap between the morphodynamics and geometries of tidal and fluvial channels.

Morphodynamic analyses of tidal and fluvial meanders reveal that tidal and fluvial channels display similar meander migration rates and meander cutoff behavior (Finotello et al. 2018; Gao et al. 2024). Width and meander wavelength of tidal channels exhibit the same linear correlation as fluvial meanders (e.g. Leopold et al., 1964), and the ratio of e-folding length for channel width to total channel length of tidal channels is similar to that of estuaries (Lanzoni and D'Alpaos, 2015; Lanzoni and Seminara, 1998; Marani et al., 2002). Statistical analyses of meanders demonstrate that meander asymmetry is a key meander metric for differentiating channel types, and that principal component analyses of meander metrics are capable of grouping tidal and fluvial reaches (Fagherazzi et al., 2004; Finotello et al., 2020).

The general overlap of morphodynamics and planform characteristics in tidal and fluvial systems, while useful for understanding hydrodynamic processes, limits our ability to classify channels as tidal or fluvial based on planform geometry. True meanders have been defined as regions of the a channel with a sinuosity index of 1.5 or greater (Leopold and Wolman, 1957). Many channel reaches have low sinuosity or broad bends that fall below this sinuosity threshold, where meander metrics do not provide the best representation. This is particularly relevant for analysis of relict channels where full or half meander geometries are not always preserved, or in cases where the relict channel has low sinuosity making application of meander metrics difficult. Multi-variate statistical analysis of meander metrics can effectively cluster longer channel reaches by channel type (Finotello et al. 2020) but this method requires the presence and delineation of meanders. Currently there is no system for classifying whole channel reaches as tidal versus fluvial that are not based on extraction of meander metrics.

Machine-learning (ML) algorithms are capable of classifying inputs based on patterns in large, high-dimensional datasets that may not be apparent using other types of analyses. These algorithms have been successfully applied to remote sensing, well log data, seismology, mining, and geologic mapping (Bressan et al., 2020; Corbi et al., 2019; Cracknell and Reading, 2014; Evans et al., 1986; El Fels and El Ghorfi, 2022; Keshtkar et al., 2017; Kong et al., 1988; Lee et al., 1994; Murti et al., 2022; Parikh et al., 2020; Wang et al., 2024). To date, however, ML methods have not been used in analysis of channel planform geometries to classify channel reaches as tidal or fluvial.

This study uses geometric analysis integrated with machine learning applied to a limited set of channel metrics to classify channels as tidal or fluvial. Our dataset consists of tidal (n = 46) and fluvial (n = 17) channels from a variety of climates, tidal ranges, channel sizes (≈ channel width), and 144 statistical variables that describe normalized width (NW), normalized curvature (NC), normalized radius of curvature (NR), convolutions of NR and NC with NW, and their derivatives. We find that dimension-reduction techniques such as linear discriminant analysis are not capable of classifying channel type based on discriminant scores. We compare the performance of three common machine-learning classification algorithms (Multi-layer Perceptron, Random Forest, and Logistic Regression) and develop thresholds for classifying individual channels as tidal or fluvial using segment-scale output of ML classifiers with reach-scale accuracies up to 100%. This method allows us to classify channels with easily extracted data from inaccessible regions on Earth, and has potential for interpreting the origin of relict channels on inactive geomorphic surfaces. Our results

show that machine-learning algorithms, particularly Random Forest classifiers, are highly accurate for classifying entire channel reaches.

METHODS

Methods used in this study can be grouped into six components: (1) digitize channel and extract a centerline; (2) calculate along-channel metrics; (3) extract statistics and segment the data; (4) train classification algorithms; (5) apply classifiers to the reach scale; and (6) Linear Discriminant Analysis (LDA). Figure 2 is a flowchart showing the complete workflow, from channel digitization to evaluation of performance for each classifier at the reach scale. The data and training scripts used in this study are available in the Tidal and Fluvial Channel Classification repository at https://osf.io/ah46v/

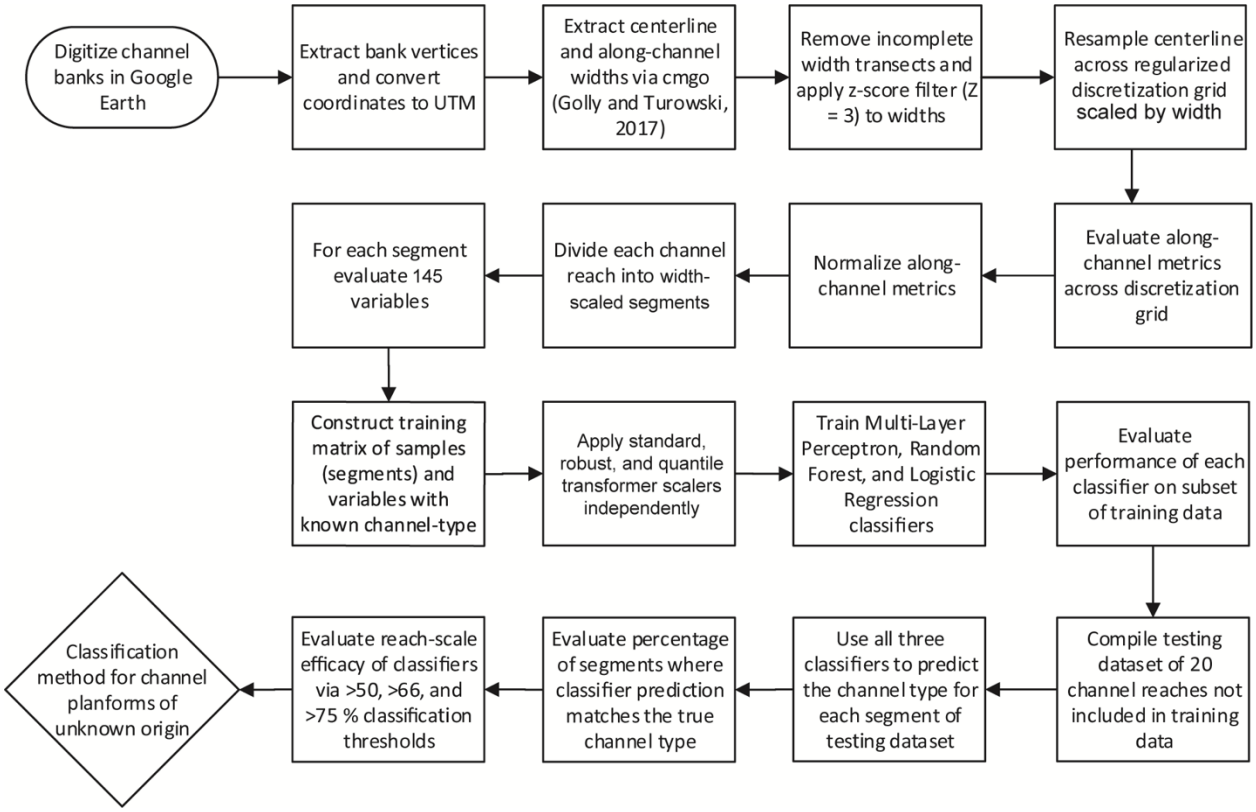

Figure 2: Flowchart illustrating the workflow for digitizing channels, extracting channel metrics, preparing datasets for input into machine-learning algorithms, training and evaluating classifier performances, and classifying at the reach scale.

1. Channel bank digitization and centerline extraction

Metrics for local channel width and curvature along a channel centerline are needed to fully capture the planform geometry of a channel reach (e.g., Vermeulen et al., 2016). We used digitized channel banks to extract a centerline along the channel reach and measure width transects across the

centerline. We digitize banks of channels at bank-full geometries in Google Earth as line objects from downstream to upstream. Nearly all channels digitized had distinct vegetation lines that we used to delineate the channel banks. In instances where vegetation was sparse, we delineated banks by clear breaks in slope on levees, manmade structures on banks, or temporal satellite imagery directly showing bankfull conditions. If channel banks could not be clearly delineated, we would select another location with clearly defined banks. We digitized channel reaches on all continents except Antarctica, cover a range of channel sizes with widths ranging from meters to hundreds of meters, and tidal ranges from micro- to macro-tidal. We then extract the coordinates of each vertex, convert them to UTM, and compile coordinates in a text file containing all bank vertices and bank-side identifiers for a given channel. To extract a centerline, we implement the R package "CMGO" (Golly and Turowski, 2017). This program uses Voronoi tessellation of channel bank vertices to establish points along the channel centerline and smooth high-frequency noise to create a smoothed centerline. At each point along the centerline, a transect perpendicular to the centerline gives the full channel width. The output of this extraction includes the coordinates of channel centerline points, distance along the channel centerline, and channel width at each point.

2. Calculate along-channel metrics

To ensure consistent measurements along a channel centerline for channels of different sizes, we re-sample the centerline across a regular discretization grid that is scaled to channel width (e.g., Fagherazzi et al., 2004; Finotello et al., 2020). We evaluate cubic spline representations of latitude, longitude, and width (w(s)) vs distance upstream at spacing equal to $1/100^{th}$ the average width of the channel reach on a discretization grid. Scaling of the discretization grid is necessary for the comparison of channels of different size and width (e.g., Finotello et al., 2024). Curvature at each point is calculated using equation 2 of Marani et al., (2003):

$$(1) \qquad c(s) = \frac{(dx/ds)(d^2y/ds^2) - (dy/ds)(d^2x/ds^2)}{[(dx/ds)^2 + (dy/ds)^2]^{3/2}}$$

where c(s) is the local channel curvature at each point along the centerline, s; x and y are longitude and latitude; dx/ds, dy/ds, d^2x/ds^2 , and d^2y/ds^2 are the first and second derivatives of x and y with respect to distance along the channel (s). Using the local channel curvature at each point, we can evaluate the local radius of curvature using the following equation:

$$(2) \qquad R(s) = \frac{1}{|c(s)|}$$

where R(s) is the radius of curvature at each point s, evaluated by taking the inverse of the absolute value of curvature at that point. To compare channels of different scales to one another, the data are normalized using the following equations:

$$NW(s) = {}^{W(s)}/_{\overline{W}} \quad (3)$$

$$NC(s) = C(s) * \overline{W} \quad (4)$$

$$NR(s) = {}^{R(s)}/_{\overline{W}} \quad (5)$$

where NW(s), NC(s), and NR (s) are normalized width, normalized curvature, and normalized radius of curvature at each point; and $\overline{W}$, $\bar{C}$ are the average width and average curvature for the entire channel reach. Finotello et al. (2020) normalized width against average width of the meander rather than the entire reach. While this method keeps variables directly related to meanders, the broader context relative to the rest of the channel reach is lost. In tidal channels that exhibit unique funneling in the downstream direction (Lanzoni and D'Alpaos, 2015; Marani et al., 2002), our approach of normalizing channel width relative to the reach-averaged width allows us to capture width anomalies that would otherwise be lost if width values were normalized to the average width of a segment, as is necessary when using meander-based metrics and segmentation. Similarly, normalizing curvature to the average curvature of the entire reach provides spatial context that would be lost if curvature was normalized against local averages.

In addition, we calculated the convolution of normalized curvature and normalized radius of curvature with width. Convolving the signals provides a measure of the effect that channel width has on curvature and radius of curvature. The discrete linear convolution is described by the equations:

$$NCxNW(s) = \sum_{m=0}^{i} NC_m NW_{s-m} \quad (6)$$

$$NRxNW(s) = \sum_{m=0}^{i} NR_m NW_{s-m} \quad (7)$$

where NCxNW and NRxNW are the convolutions of normalized curvature and normalized radius of curvature with normalized width, m is the point along the NC or NR signal, i is the end point of the signal, and S is the point along the width signal. To better capture how geometry changes along the centerline, we also calculate the first derivative with respect to s for normalized width, normalized curvature, normalized radius of curvature, NCxNW, and NRxNW. Additionally, we utilize the simple quotient of normalized curvature and normalized width, given by the equation:

$$NC/NW = \frac{NC}{NW} \quad (8)$$

where NC/NW is the normalized curvature to normalized width ratio, NC is normalized curvature, and NW is normalized width. At this step, each point along the centerline of each channel reach has

a measure of normalized width, normalized curvature, normalized radius of curvature, normalized curvature convolved with normalized width, normalized radius of curvature convolved with normalized width, the first derivatives of these signals. These metrics provide the basis for all statistical analyses and variables used in the training and testing datasets.

3. Extract statistics and segment the data

Each channel reach is divided into uniform segments, where each segment is treated as an individual sample described by statistical measures of NW, NC, NR, NCxNW, NRxNW, and NCWR. Segmentation is necessary to capture local geometric details that may be important for distinguishing tidal versus fluvial channel types, though choosing a segment size that is too small may result in overfitting to high-frequency noise that inhibits classification. Many tidal channels are short (~ 1 km), which means assigning segments that are too long results in loss of local detail. This requires more tidal channels to be digitized to achieve a balance in the number of segments from fluvial and tidal channels. In this study, we divide all channel reaches into segments scaled to double the average channel width, to maximize coverage of tidal channels and minimize overfitting of noise on larger channels. This approach is different from previous studies which segmented channels based on the delineation of individual meander bends.

For each channel segment we calculate thirteen statistical variables (Table 1). For each of the eleven along-channel metrics (NCWR, NW, NC, NR, NCxNW, NRxNW, NW', NC', NR', NCxNW', NRxNW') we calculate the mean, variance, standard deviation, minimum, maximum, median, midpoint, skewness, kurtosis, range, mean absolute deviation, intra-quartile range, and mode. In addition to these 143 statistical variables, we also calculate the sinuosity of each channel segment for a total of 144 variables with the following equations:

$$L_c = \sqrt{\left(x_{last} - x_{first}\right)^2 + \left(y_{last} - y_{first}\right)^2} \quad (9)$$

$$SI = \frac{L_s}{L_c} \quad (10)$$

where L_c is the cartesian distance between the first and last points in the segment, x and y are the longitude and latitude of the first and last points, L_s is the intrinsic distance along the centerline of the segment, and SI is the sinuosity index. This provides a measure of the degree to which a particular segment is meandering or straight.

We completed this process for tidal (n = 46) and fluvial channels (n = 17) that were used to train and evaluate the classifiers, and to 20 additional tidal (n =10) and fluvial channels (n = 10) used to test the accuracy of the classifiers at the reach scale. The final training dataset contains 4294 fluvial and tidal channel segments, each with 145 variables describing their geometries and class labels (tidal or fluvial).

Table 1: List of along-channel metrics and statistical variables extracted from each channel segment.

Metric	Variables
Normalized Curvature/Normalized Width (=NC/NW)	$\overline{\text{NC/NW}}$, $\boldsymbol{\sigma}_{\text{NC/NW}}$, $\boldsymbol{\sigma^2}_{\text{NC/NW}}$, $\boldsymbol{Min}_{\text{NC/NW}}$, $\boldsymbol{Max}_{\text{NC/NW}}$, $\text{Mid}_{\text{NC/NW}}$, $\boldsymbol{Me}_{\text{NC/NW}}$, $\boldsymbol{\gamma}_{\text{NC/NW}}$, $\boldsymbol{\kappa}_{\text{NC/NW}}$, $\text{Range}_{\text{NC/NW}}$ $\text{MAD}_{\text{NC/NW}}$, $\text{IQR}_{\text{NC/NW}}$, $\text{Mode}_{\text{NC/NW}}$
Normalized Width (= NW)	$\overline{\text{NW}}$, $\boldsymbol{\sigma_{NW}}$, $\boldsymbol{\sigma^2_{NW}}$, $\boldsymbol{Min_{NW}}$, $\boldsymbol{Max_{NW}}$, $\text{Mid}_{\boldsymbol{NW}}$, $\boldsymbol{Me_{NW}}$, $\boldsymbol{\gamma_{NW}}$, $\boldsymbol{\kappa_{NW}}$, $\text{Range}_{\boldsymbol{NW}}$, $\text{MAD}_{\boldsymbol{NW}}$, $\text{IQR}_{\boldsymbol{NW}}$, $\text{Mode}_{\boldsymbol{NW}}$
Normalized Curvature (= NC)	$\overline{\text{NC}}$, $\boldsymbol{\sigma_{NC}}$, $\boldsymbol{\sigma^2_{NC}}$, $\boldsymbol{Min_{NC}}$, $\boldsymbol{Max_{NC}}$, $\text{Mid}_{\boldsymbol{NC}}$, $\boldsymbol{Me_{NC}}$, $\boldsymbol{\gamma_{NC}}$, $\boldsymbol{\kappa_{NC}}$, $\text{Range}_{\boldsymbol{NC}}$, $\text{MAD}_{\boldsymbol{NC}}$, $\text{IQR}_{\boldsymbol{NC}}$, $\text{Mode}_{\boldsymbol{NC}}$
Normalized Radius of Curvature (= NR)	$\overline{\text{NR}}$, $\boldsymbol{\sigma_{NR}}$, $\boldsymbol{\sigma^2_{NR}}$, $\boldsymbol{Min_{NR}}$, $\boldsymbol{Max_{NR}}$, $\text{Mid}_{\boldsymbol{NR}}$, $\boldsymbol{Me_{NR}}$, $\boldsymbol{\gamma_{NR}}$, $\boldsymbol{\kappa_{NR}}$, $\text{Range}_{\boldsymbol{NR}}$, $\text{MAD}_{\boldsymbol{NR}}$, $\text{IQR}_{\boldsymbol{NR}}$, $\text{Mode}_{\boldsymbol{NR}}$
NC convolved with NW (= NCxNW)	$\overline{\text{NCxNW}}$, $\boldsymbol{\sigma_{NCxNW}}$, $\boldsymbol{\sigma^2_{NCxNW}}$, $\boldsymbol{Min_{NCxNW}}$, $\boldsymbol{Max_{NCxNW}}$, $\text{Mid}_{\boldsymbol{NCxNW}}$, $\boldsymbol{Me_{NCxNW}}$, $\boldsymbol{\gamma_{NCxNw}}$, $\boldsymbol{\kappa_{NCxNW}}$, $\text{Range}_{\boldsymbol{NCxNW}}$, $\text{MAD}_{\boldsymbol{NCxNW}}$, $\text{IQR}_{\boldsymbol{NCxNW}}$, $\text{Mode}_{\boldsymbol{NCxNW}}$
NR convolved with NW (= NRxNW)	$\overline{\text{NRxNW}}$, $\boldsymbol{\sigma_{NRxNW}}$, $\boldsymbol{\sigma^2_{NRxNW}}$, $\boldsymbol{Min_{NRxNW}}$, $\boldsymbol{Max_{NRxNW}}$, $\text{Mid}_{\boldsymbol{NRxNW}}$, $\boldsymbol{Me_{NRxNW}}$, $\boldsymbol{\gamma_{NRxNW}}$, $\boldsymbol{\kappa_{NRxNW}}$, $\text{Range}_{\boldsymbol{NRxNW}}$, $\text{MAD}_{\boldsymbol{NRxNW}}$, $\text{IQR}_{\boldsymbol{NRxNW}}$, $\text{Mode}_{\boldsymbol{NRxNW}}$
$\boldsymbol{dNW/ds}$ (= NW')	$\overline{\text{NW}}'$, $\boldsymbol{\sigma_{NW'}}$, $\boldsymbol{\sigma^2_{NW'}}$, $\boldsymbol{Min_{NW'}}$, $\boldsymbol{Max_{NW'}}$, $\text{Mid}_{\boldsymbol{NW'}}$, $\boldsymbol{Me_{NW'}}$, $\boldsymbol{\gamma_{NW'}}$, $\boldsymbol{\kappa_{NW'}}$, $\text{Range}_{\boldsymbol{NW'}}$, $\text{MAD}_{\boldsymbol{NW'}}$, $\text{IQR}_{\boldsymbol{NW'}}$, $\text{Mode}_{\boldsymbol{NW'}}$
$\boldsymbol{dNC/ds}$ (= NC')	$\overline{\text{NC}}'$, $\boldsymbol{\sigma_{NC'}}$, $\boldsymbol{\sigma^2_{NC'}}$, $\boldsymbol{Min_{NC'}}$, $\boldsymbol{Max_{NC'}}$, $\text{Mid}_{\boldsymbol{NC'}}$, $\boldsymbol{Me_{NC'}}$, $\boldsymbol{\gamma_{NC'}}$, $\boldsymbol{\kappa_{NC'}}$, $\text{Range}_{\boldsymbol{NC'}}$, $\text{MAD}_{\boldsymbol{NC'}}$, $\text{IQR}_{\boldsymbol{NC'}}$, $\text{Mode}_{\boldsymbol{NC'}}$
$\boldsymbol{dNR/ds}$ (= NR')	$\overline{\text{NR}}'$, $\boldsymbol{\sigma_{NR'}}$, $\boldsymbol{\sigma^2_{NR'}}$, $\boldsymbol{Min_{NR'}}$, $\boldsymbol{Max_{NR'}}$, $\text{Mid}_{\boldsymbol{NR'}}$, $\boldsymbol{Me_{NR'}}$, $\boldsymbol{\gamma_{NR'}}$, $\boldsymbol{\kappa_{NR'}}$, $\text{Range}_{\boldsymbol{NR'}}$, $\text{MAD}_{\boldsymbol{NR'}}$, $\text{IQR}_{\boldsymbol{NR'}}$, $\text{Mode}_{\boldsymbol{NR'}}$
$\boldsymbol{dNCxNW/ds}$ (= NCxNW')	$\overline{\text{NCxNW}}'$, $\boldsymbol{\sigma_{NCxNW'}}$, $\boldsymbol{\sigma^2_{NCxNW'}}$, $\boldsymbol{Min_{NCxNW'}}$, $\boldsymbol{Max_{NCxNW'}}$, $\text{Mid}_{\boldsymbol{NCxNW'}}$, $\boldsymbol{Me_{NCxNW'}}$, $\boldsymbol{\gamma_{NCxNW'}}$, $\boldsymbol{\kappa_{NCxNW'}}$, $\text{Range}_{\boldsymbol{NCxNW'}}$, $\text{MAD}_{\boldsymbol{NCxNW'}}$, $\text{IQR}_{\boldsymbol{NCxNW'}}$, $\text{Mode}_{\boldsymbol{NCxNW'}}$
$\boldsymbol{dNRxNW/ds}$ (= NRxNW')	$\overline{\textbf{NRxNW}}'$, $\boldsymbol{\sigma_{NRxNW'}}$, $\boldsymbol{\sigma^2_{NRxNW'}}$, $\boldsymbol{Min_{NRxNW'}}$, $\boldsymbol{Max_{NRxNW'}}$, $\text{Mid}_{\boldsymbol{NRxNW'}}$, $\boldsymbol{Me_{NRxNW'}}$, $\boldsymbol{\gamma_{NRxNW'}}$, $\boldsymbol{\kappa_{NRxNW'}}$, $\text{Range}_{\boldsymbol{NR'xNW}}$, $\text{MAD}_{\boldsymbol{NRxNW'}}$, $\text{IQR}_{\boldsymbol{NRxNW'}}$, $\text{Mode}_{\boldsymbol{NRxNW'}}$
Sinuosity	**SI**

d/ds = first derivative of metric with respect to distance upstream (s); Me = Median; MAD = Mean Absolute Deviation; IQR = Intra-Quartile Range, γ = skewness; κ = kurtosis

(4) Train classification algorithms

To determine the most effective machine-learning algorithm, we trained and tested three different supervised classification algorithms using the scikit-learn package in Python: Logistic Regression, Multi-layer Perceptron, and Random Forest (Pedregosa et al., 2011). The Logistic Regression (LR) classifier is a simple classifier that creates a linear combination of variables, passes it through a sigmoid function, and returns the probability of it being one class or the other

(McCullagh, 2019). LR classification has been successfully implemented for land cover classification using multispectral data (Das and Pandey, 2019). The Multi-layer Perceptron (MLP) is a form of neural network that takes the input variables, connects them to a pre-defined structure of layered nodes where it determines connection weights between layers, and outputs the predicted class nodes. The MLP algorithm then compares its predictions to the true values, and adjusts the node connection weights via backpropagation and stochastic optimization to determine the optimal weights with the highest accuracy (Hinton, 1990; Kingma and Ba, 2014). Random Forest classifiers are comprised of bootstrap aggregated decision trees (**Figure 3**) where each node at a split is chosen based on the greatest split between the classes, and the final output of the classifier is democratically chosen by all individual trees via majority vote (Breiman, 2001).

Prior to training we defined the structure the Multi-layer Perceptron where each hidden layer has half the number of nodes (rounded to the nearest integer) of the preceding layer. (Kingma and Ba, 2014). The number of hidden layers is determined by the last hidden layer to have more than 2 nodes. We applied an alpha of 0.001, the rectified linear unit activation function and the *adam* stochastic optimization solver to the MLP model (e.g., Kingma and Ba (2014)). The Random Forest classifier was structured with 100 decision trees in the forest, using gini impurity to determine the split quality. We applied the 'sag' solver, which is well suited for large datasets with binary labels. Each classifier was trained on the training dataset of 4294 tidal and fluvial segments, where 80% of the data was used to train the models and the remaining 20% was reserved for testing segment-scale accuracy.

(5) Apply classifiers to the reach scale

Each of the classifiers above was trained to classify channels at the segment scale, thus giving the classifiers enough geometric data to provide robust classifications. However, classifying a single segment is not sufficient to classify an entire reach as tidal versus fluvial. The classification of all segments within a reach must also be considered to classify the full reach. To address this, we implemented three classification thresholds th

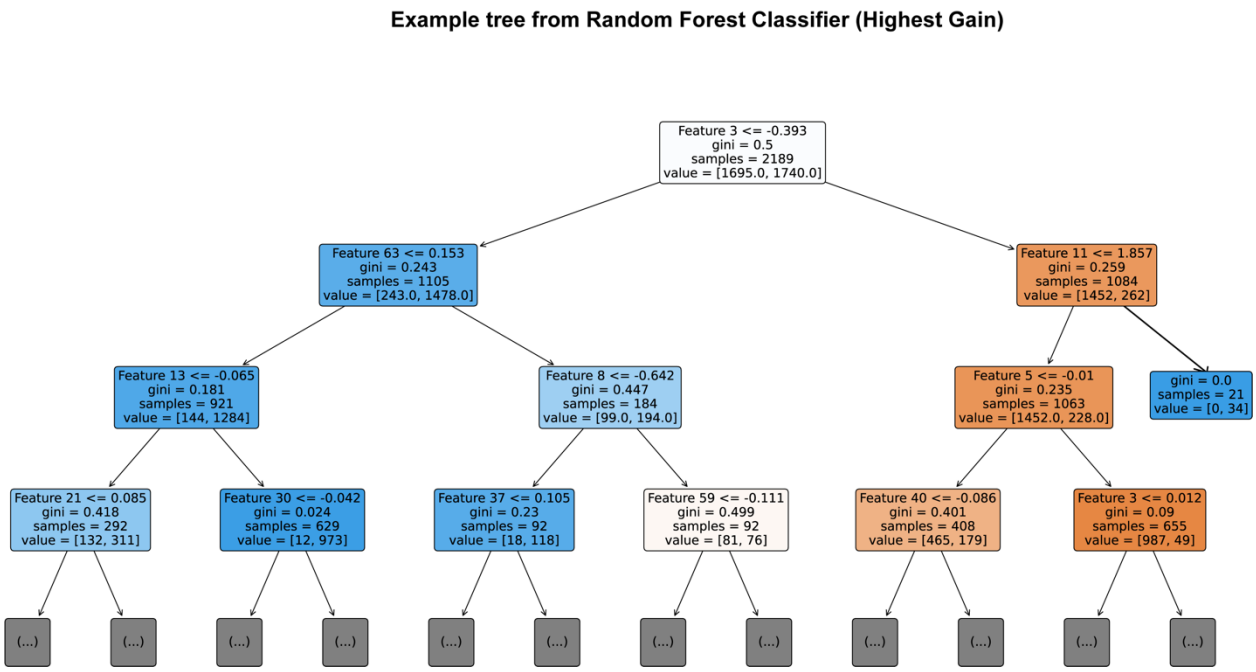

Figure 3: Example tree from the Random Forest Classifier chosen by highest gain levels. Blue leaves are dominated by tidal samples while red leaves are dominated by fluvial samples. Each leaf represents a feature variable and threshold values. Only 3 full levels are shown. Nodes on the far right exemplify end results of purely tidal or purely fluvial nodes.

at represent the percent of segments in a reach needed to classify the channel as tidal or fluvial: >50%, >66%, and >75%. In all cases, the dominant segment type determines the channel type, but the majority needed increases with increased classification threshold. To assess the efficacy of each classifier at these thresholds, we presented the trained models with a separate dataset of ten tidal and ten fluvial channel reaches prepared identically to our training dataset. The models classify all segments within a reach as either tidal or fluvial. For each channel reach, we evaluate the number of tidal segments and fluvial segments and classify the reach as the dominant channel type determined at each threshold. The accuracy of a classifier is determined by the percent of reaches that were correctly classified (e.g. tidal reach was classified as tidal). The classifier that had the highest overall reach-scale accuracy and the smallest decrease in accuracy with an increased classification threshold was considered to be the best performing.

To maximize performance of the classifiers at the reach scale, we performed 69 training trials on each classifier. We organized variables that were included in each trial into 23 different configurations ranging from all the variables to only small subsets of the data (Table 2), and ran each metric configuration through three different scalers in the scikit-learn library: standard scaler (parametric), robust scaler (non-parametric), and quantile transformer (non-parametric) (Pedregosa et al., 2011). By adjusting these two parameters we can understand the effects of different groupings

of data on the performance of these classifiers. This approach also reveals how the different combinations are affected by parametric and non-parametric scaling.

Table 2: 23 Principal along-channel metric configurations used in this study.

MC	NC/NW	NW	NC	NR	NCxNW	NRxNW	NW'	NC'	NR'	NCxNW'	NRxNW'	SI
1	Y	Y	Y	Y	Y	Y	Y	Y	Y	Y	Y	Y
2	Y	Y	Y	Y	Y	Y	Y	Y	Y	Y	Y	N
3	N	Y	Y	Y	Y	Y	Y	Y	Y	Y	Y	Y
4	N	Y	Y	Y	Y	Y	Y	Y	Y	Y	Y	N
5	Y	Y	Y	Y	Y	Y	N	N	N	N	N	Y
6	N	Y	Y	Y	Y	Y	N	N	N	N	N	Y
7	N	Y	Y	Y	Y	Y	N	N	N	N	N	N
8	Y	N	N	N	N	N	Y	Y	Y	Y	Y	Y
9	Y	N	N	N	N	N	Y	Y	Y	Y	Y	N
10	N	N	N	N	N	N	Y	Y	Y	Y	Y	N
11	N	N	N	N	N	N	Y	Y	Y	Y	Y	Y
12	Y	N	N	N	Y	Y	N	N	N	Y	Y	Y
13	Y	N	N	N	Y	Y	N	N	N	Y	Y	N
14	N	N	N	N	Y	Y	N	N	N	Y	Y	N
15	N	N	N	N	Y	Y	N	N	N	Y	Y	Y
16	Y	Y	Y	N	Y	N	Y	Y	N	Y	N	Y
17	Y	Y	Y	N	Y	N	Y	Y	N	Y	N	N
18	N	Y	Y	N	Y	N	Y	Y	N	Y	N	N
19	N	Y	Y	N	Y	N	Y	Y	N	Y	N	Y
20	Y	Y	N	Y	N	Y	Y	N	Y	N	Y	Y
21	Y	Y	N	Y	N	Y	Y	N	Y	N	Y	N
22	N	Y	N	Y	N	Y	Y	N	Y	N	Y	N
23	N	Y	N	Y	N	Y	Y	N	Y	N	Y	Y

Legend: MC = Metric Configuration; Y = Principal metric (and variables) included in this configuration; N= Principal metric (and variables) excluded in this configuration. NC/NW = Normalized curvature/normalized width; NW = Normalized width, NC = normalized curvature; NR = normalized radius of curvature; NCxNW = convolution of NC with NW; NRxNW = convolution of NR with NW; SI = sinuosity index; ' = first derivative of the principal metric with respect to distance along the channel centerline.

(6) Linear Discriminant Analysis (LDA)

A simple form of supervised classification is linear discriminant analysis (LDA). Given classified data and variables, LDA transforms data to maximize between-class variance and minimize within-class variance. In doing so, the LDA creates the greatest possible separation between the discriminant scores of each group. Discriminant scores are best used to classify data when a clear threshold score is defined that separates the classes. We performed a linear discriminant analysis on our training dataset of 4294 fluvial and tidal channel segments, and the results are presented below.

RESULTS

Linear Discriminant Analysis

Figure 4 shows the frequency distribution and violin plots of discriminant scores for fluvial and tidal channel segments. The range of discriminant score values overlaps significantly for the two groups, which means there is no threshold discriminant score with which to separate the groups. The discriminant scores for fluvial channel segments do not exceed 2, whereas there are several tidal channel segments that are above this score, suggesting that segments with scores above this can be classified as tidal. However, results of the Linear Discriminant Analysis are not sufficient to classify channel segments as tidal or fluvial, prompting the need for more powerful classifiers.

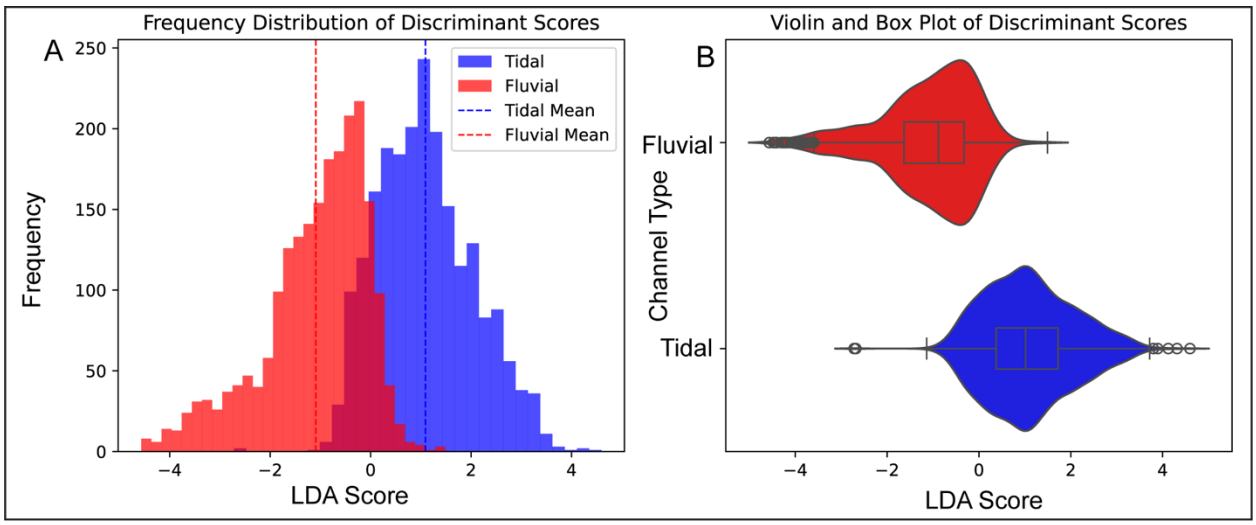

Figure 4: Plots of discriminant scores for tidal and fluvial segments derived from linear discriminant analysis. A) Frequency distribution and means for tidal and fluvial discriminant scores; B) Combined violin and box plots for tidal and fluvial discriminant scores displaying overlap of the intraquartile range for both distributions, and a larger number of outliers for the tidal distribution. There is considerable overlap between the two populations. The distribution of fluvial discriminant scores is negatively skewed while the distribution of tidal discriminant scores is positively skewed. No clear threshold score for differentiating between the groups could be identified.

Segment-scale Classifier Performance

The classifiers used in this study operate at the segment scale ($L_s = 2\overline{W}$), where L_s is the segment length for a given channel and $\overline{W}$ is the average width of the channel, and therefore the most direct assessment of the classifiers is their accuracy in classifying segments. Across 69 trials the Logistic Regression classifier performed the worst, with accuracies ranging from 64% to 90% (mean = 80%). The Multi-layer Perceptron classifier performed significantly better than the Logistic Regression classifier, with accuracies ranging from 82% to 95% (mean = 89%). The best and most

consistent performance across all trials was the Random Forest classifier with segment-scale accuracies between 89% and 97% (mean = 93%) (See Supplementary File S1)

Figure 5 shows important segment-scale performance metrics for the Random Forest

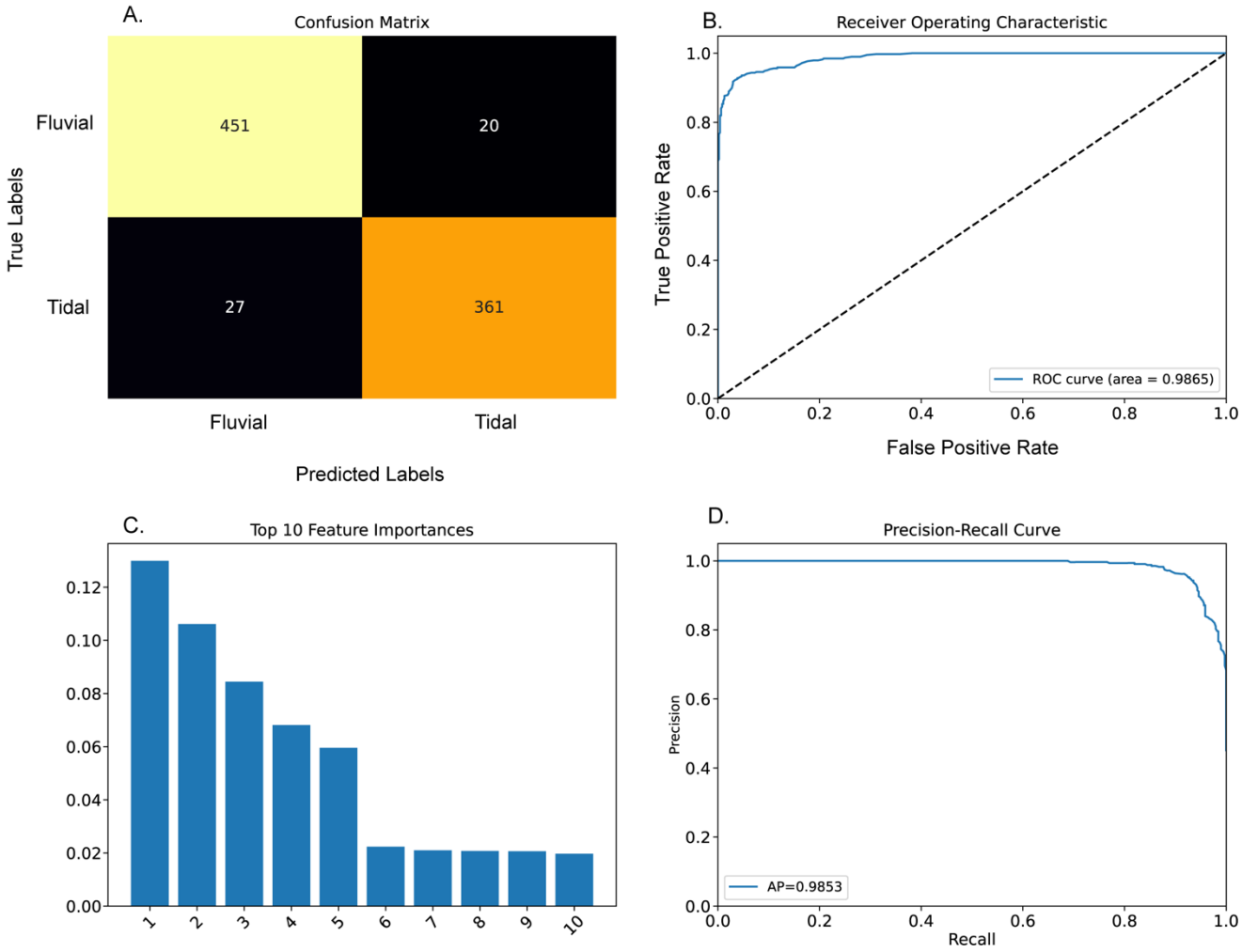

Figure 5: Composite Evaluation of Random Forest Classifier. A) The confusion matrix demonstrates dominantly true positives (tidal) and negatives (fluvial) with fewer false positives and false negatives. B) The ROC curve suggests a high true positive rate with few false positives. C) The feature importance bar chart ranks the top 10 predictors (full feature names are in Table 3), with height representing relative importance. Note that the top 5 are significantly more important than 6-10. D) Precision recall curve indicating high precision at various recall thresholds. Precision drops sharply as recall approaches 1, as the model becomes less conservative at these thresholds

classifier that performed the best at the reach scale (trial 58). The confusion matrix (Fig. 5a) shows that the Random Forest classifier successfully predicted 451 true fluvial segments and 361 true tidal segments, while misclassifying 27 true tidal segments and 20 true fluvial segments with overall segment scale accuracy of 95%. The Receiver Operating Characteristic (ROC) curve (Figure 5b) is a plot of the true positive rate against the false positive rate and shows an area under the curve (AUC) of 0.9865. This near-perfect score indicates an exceptional level of discrimination between classes. The feature importances chart (Figure 5c) shows the top 10 statistical variables, ranked by importance, used to discriminate between classes (Full rankings in Supplementary File S2). Table 3 shows these same rankings with the full names of the top 10 statistical variables included. Statistical variables describing the central tendency and the minimum and maximum of the convolution of normalized radius of curvature with normalized width (NRxNW) comprise the top 5 most important features, with importances at least twice that of the next highest ranked variables. The lowest ranked variable (Rank 88) is the variance of the derivative of normalized radius of curvature with respect to s. The Precision-Recall curve (Figure 5d) is a plot of precision (the proportion of true tidal segments among all segments) versus recall (the proportion of true tidal segments among all actual tidal segments) at different threshold settings. We have an average precision value (AP) of 0.9853, which indicates that the classifier has high precision across a wide range of recall values. Only when the model approaches recall values near 1.0 do we observe a significant drop-off in the precision values, which is expected because the classifier becomes less conservative as it boosts recall, increasing the number of false positives.

Collectively, these results demonstrate that the Random Forest classifier performs exceptionally well at the segment scale, maintaining high accuracies relative to the MLP and Logistic Regression classifier, as well as a high ROC area and Average Precision.

Reach-scale Classifier Performance

The performance of individual classifiers at the reach scale using segment-scale data is a key factor in determining the most effective classifier and classification threshold for unknown channel reaches. **Figure 6** shows example centerlines for one fluvial channel and one tidal channel, with segments color-coded according to their predicted type from the Random Forest classifier. We presented trained classifier models with previously unseen datasets for 10 tidal and 10 fluvial channels. In 69 trials comparing data scalers and metric configurations, we evaluated the performance of trained models at the reach scale by the percent of channel reaches correctly classified at three classification thresholds using the segment-scale output of the classifiers for a given reach. **Figure 7** is a heatmap showing the accuracy of each classifier at the reach scale for three thresholds, along with the metric configuration and scaler associated with each trial. At the highest classification threshold (>75%), the Logistic Regression classifier had reach-scale accuracies ranging from 25% to 80%, the MLP

classifier had reach-scale accuracies of 45% to 80%, and the Random Forest classifier had accuracies between 65% and 80%. At the >66% classification threshold, we observe the following ranges of reach-scale accuracies for each classifier: Logistic Regression = 50% to 85%; MLP classifier = 60% to 90%; and Random Forest classifier = 75% to 95%. The Random Forest classifier had the best performance, followed closely by the MLP classifier, and the Logistic Regression classifier had the worst performance. The >50% classification threshold produced the best reach-scale performance, with the following accuracies for each classifier: Logistic Regression = 70% to 95%; MLP classifier = 75% to 100%; and Random Forest classifier = 85% to 100%. At this classification threshold, all classifiers achieved 95% or greater reach-scale accuracy on one or more trials. Major differences in performance for this threshold can be seen in the minimum accuracies for each classifier, where the Random Forest classifier had the greatest minimum accuracy, the MLP had the second greatestminimum accuracy, and the Logistic Regression had the lowest minimum accuracy.

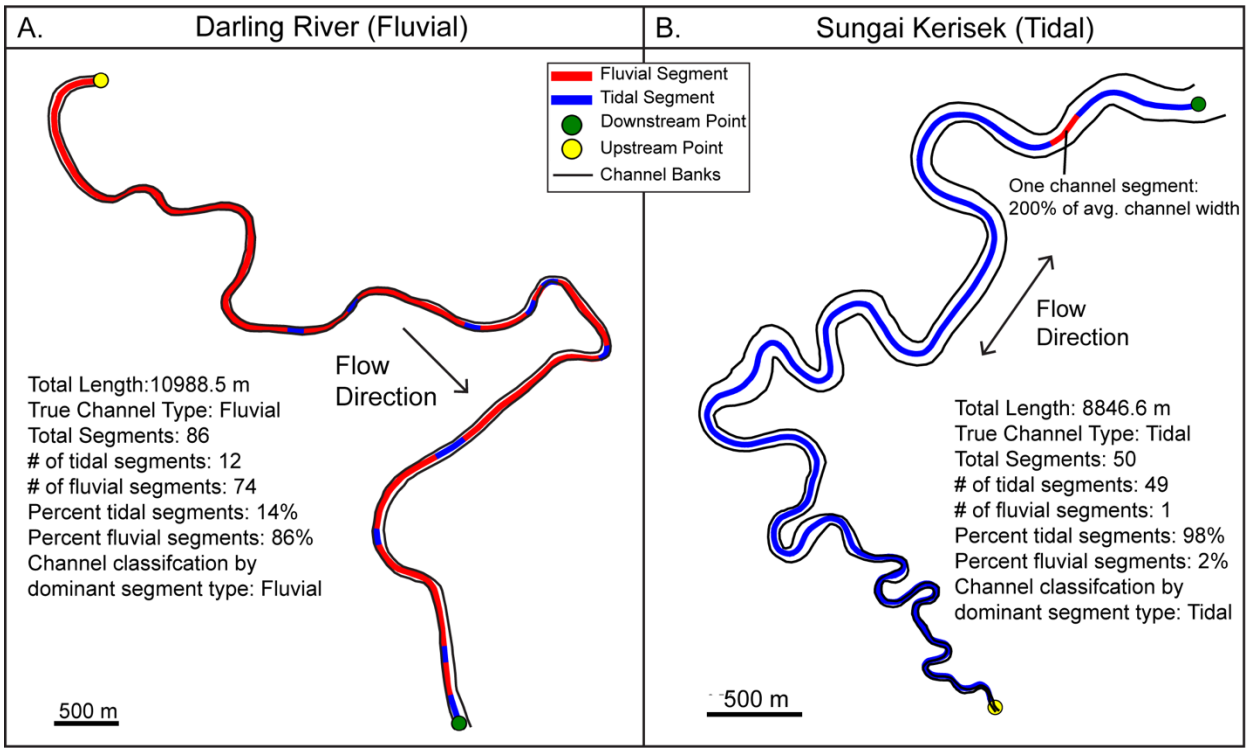

Figure 6: Classified centerlines for two example channels classified using the Random forest classifier and configurations from trial 58: A) Darling river (fluvial), and B. Sungai Kerisek (tidal). Additional information about the length of the reach, number of segments, classification of segments, and classification of the entire channel reach.

The heatmap in Figure 7 highlights the broad pattern of results observed throughout the trials. Reach-scale accuracy generally decreased with higher classification thresholds, except in some

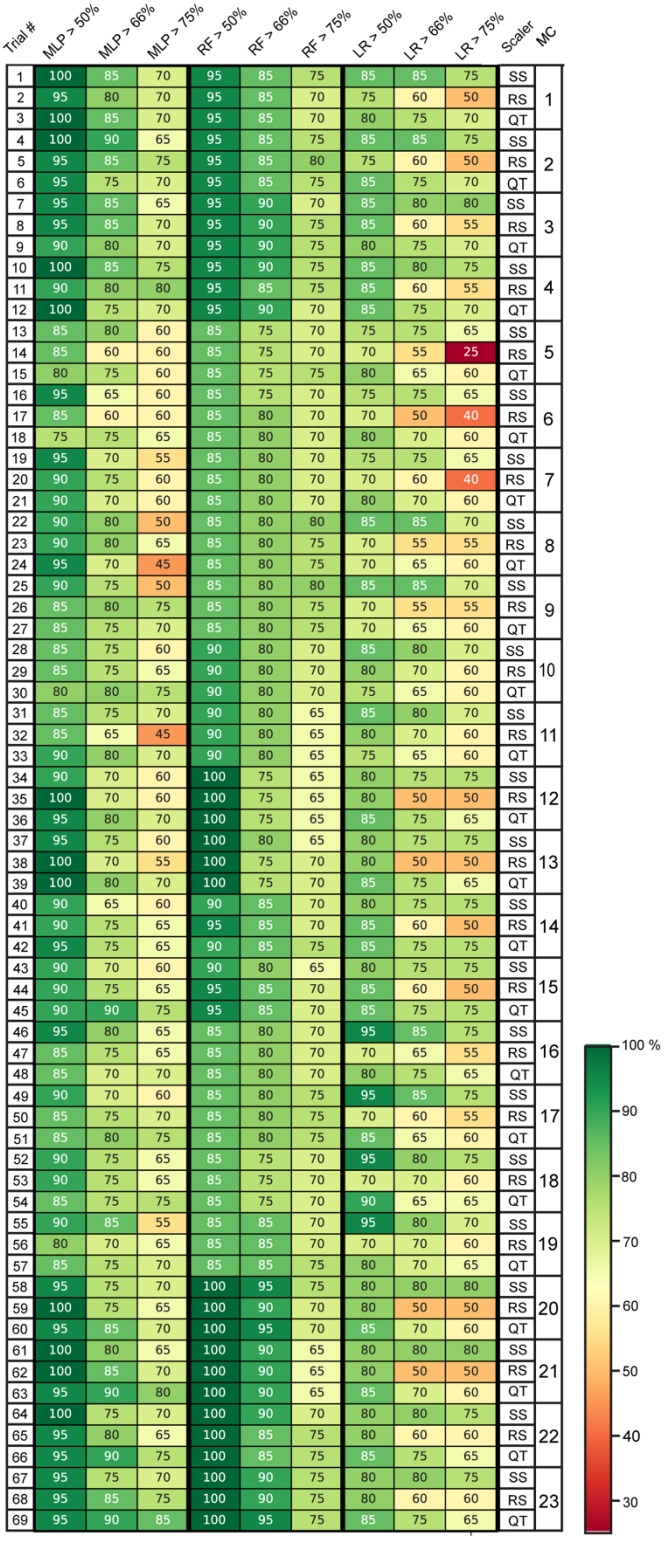

instances where there was no decrease at higher classification thresholds. For any given trial, no classifier had an increase in reach-scale accuracy as the classification threshold was increased. All classifiers had either decreased or unchanged accuracy with increasing classification thresholds. In most trials, the Logistic Regression classifier performed the worst in comparison to the other two. The Logistic Regression classifier had its best performance in trials 46 and 49 where it achieved 95%, 85%, and 75% reach-scale accuracy for each classification threshold, respectively. The Multi-layer Perceptron classifier reached its peak performance in trial 4, where it had 100%, 90%, and 65% reach-scale accuracies at the respective classification thresholds. The Random Forest classifier outperformed the other two classifiers in trials 58 and 69, where it achieved 100%, 95%, and 75% reach-scale accuracies at the three classification thresholds. Both trials exclude statistical variables from NC, NCxNW, NC', and NCxNW', but trial 58 includes NC/NW whereas trial 68 excludes those variables. Another key difference is that trial 58 uses the standard scaler from sci-kit learn, and

Figure 7: Heatmap showing the reach scale accuracy for Logistic Regression (LR), NN (Neural Network - MLP), and Random Forest (RF) classifiers at three classification thresholds (>50%, >66%, >75%). Each row represents a different trial consisting of different combinations of feature variables and scalers. See table in supplementary file S2 for variables used. MC = Metric Configuration; SS = Standard Scaler; RS = Robust Scaler; QT = Quantile Transformer

trial 69 uses the quantile transformer from sci-kit learn. The metric configuration and classifier used in trial 58 has advantages over that of trial 69, despite identical performance. The quantile transformer is a non-linear transformation of input data that suppresses outliers, but it makes interpretation of feature importance difficult as the features are non-linearly related to their original values. Trial 58 uses the standard scaler, a linear transformation, enabling straightforward interpretation of feature importance rankings via preservation of linear relationships variables. As there is no sacrifice in reach-scale accuracy by retaining data interpretability, the Random Forest classifier in trial 58 represents the most successful configuration.

Reach Classification using Random Forest Classifier

Figure 8 shows centerlines for a subset of fluvial and tidal channels used in the reach-scale testing dataset. These reaches were classified with the trained Random Forest classifier using the configurations from the best performing trial (Trial 58) at the >50% threshold. Individual segments of the centerlines are color-coded to show the predicted channel types in the context of their surrounding reach. All 20 fluvial and tidal channel reaches were correctly classified using the >50% threshold.

The performance of all three classifiers for the same channels in trial 58 is shown in **Figure 9**. Each reach has three bars representing the percent of segments for which the prediction matches the true channel type, with the >50%, >66%, and >75% classification thresholds indicated. This allows direct comparison within and between classifiers and channel types. Each classifier utilizes the data differently, and therefore certain segments classified as one channel type or the other may be classified differently by another model. Normalized width and normalized curvature are the two metrics from which channel planform can be completely reconstructed (Vermeulen *et al.,* 2016). In Figure 10, these two metrics are plotted as a function of distance upstream, for one tidal channel and one fluvial channel, classified by the three classifiers. The classified segments are color-coded to show their predicted channel type. In all cases we see that no two classifiers classify the same reach identically, and that the Random Forest classifier produces the greatest number of segments that are correctly classified.

DISCUSSION

The preceding results show that modern tidal and fluvial channels can be distinguished from each other through statistical analysis of channel planform geometries using common machine-learning tools. The

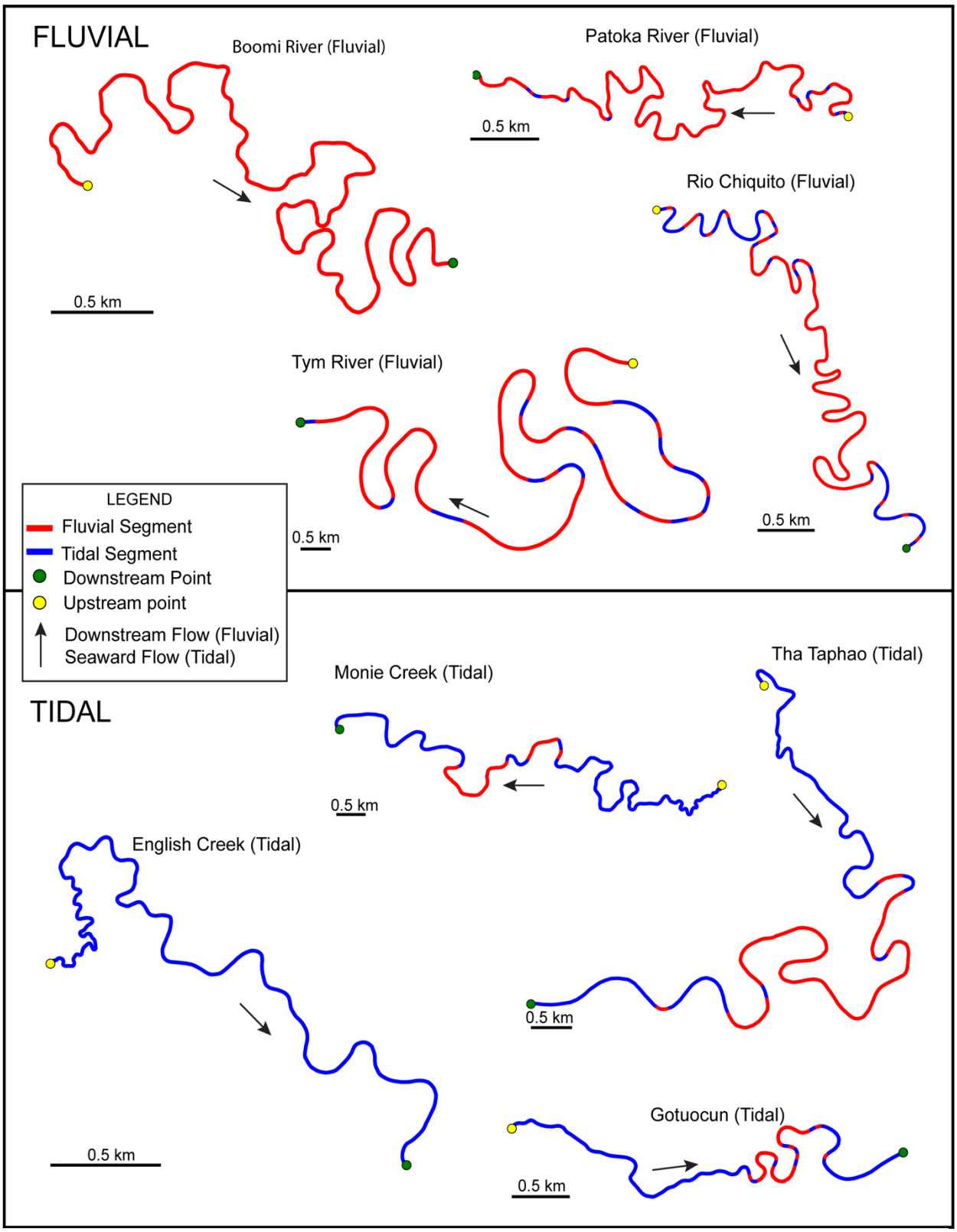

Figure 8: Classified channel centerlines for a subset of classified tidal and fluvial channels used for reach-scale testing. Classified using the trained Random Forest classifier using configurations from the best performing trial (Trial 58).

Random Forest classifier exhibited the highest accuracy levels for all three classifiers at the >50% classification threshold by application of outlier-resistant scaling methods. Below we explore four related topics: (1) application of segment-trained classifiers to larger channel reaches; (2) assessment of metric configurations; (3) feature importances and implications for differentiating channel types; and (4) implications for interpreting relict and possibly mixed-energy channel planforms.

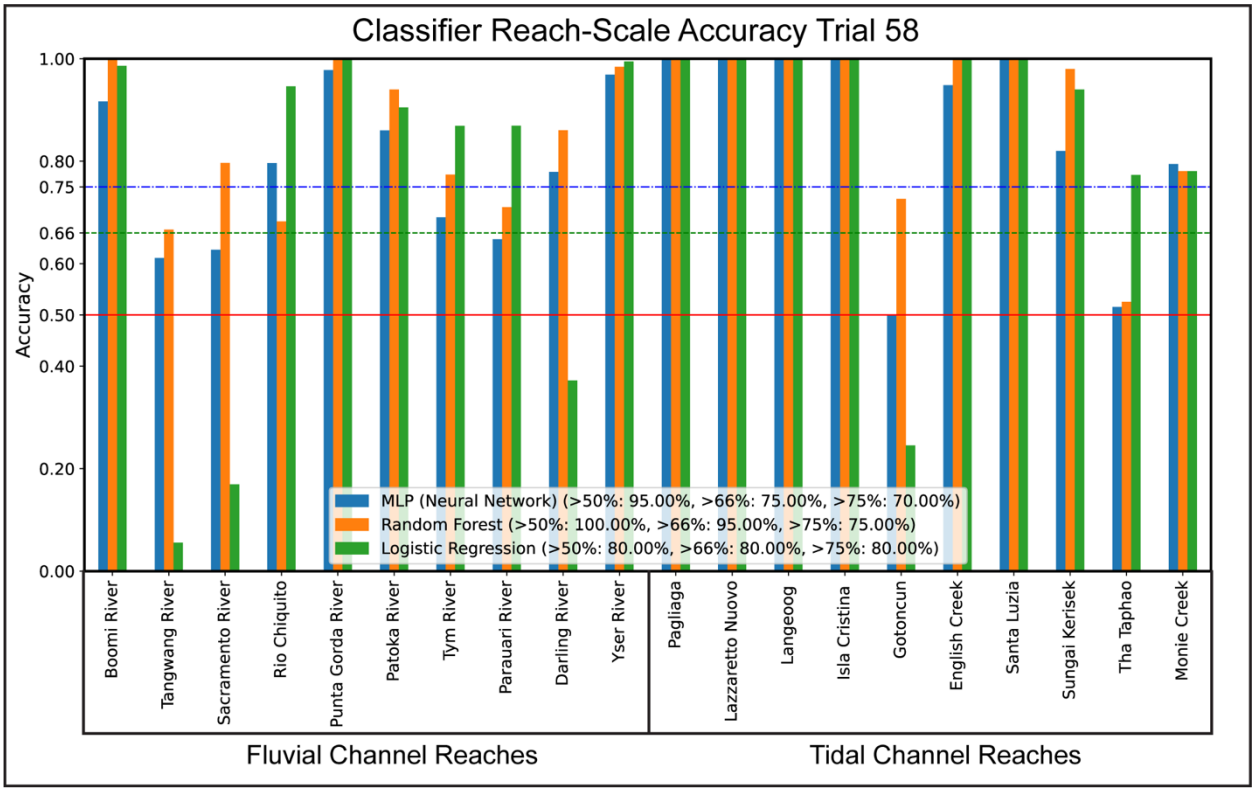

Figure 9: Bar graph comparing the reach-scale accuracy for three different classifiers: Multi-layer Perceptron (MLP), Random Forest, and Logistic Regression. 10 tidal channel reaches and 10 fluvial channel reaches were treated as unknowns by each classifier. The accuracy for each classifier for a given channel is the percentage of 100 m channel segments that were correctly classified (i.e. when the predicted channel type matches the true channel type). Three threshold levels (50%, 66%, 75%) represent the percentage of segments that must be correctly classified in order for the entire reach to be classified as that channel type. The Random Forest classifier has 100 % accuracy at correctly classifying at the reach scale for a 50% threshold, while the MLP (Neral Network) and Logistic Regression classifiers have 95% and 80% accuracy at the 50% threshold, respectively.

1. Application of segment-trained classifiers to larger channel reaches

By segmenting the data and using statistical variables to describe the geometry of each segment, we can capture local variability and preserve the geometric characteristics of upstream and downstream segments without needing to account for position within the channel or relative to adjacent segments. However, the end goal of the classification is not at the segment scale, but to perform classification of longer channel reaches. To bridge this gap, we calculate the percent of segments in a reach that are classified as tidal or fluvial to obtain a reach-scale classification, without having the classifiers classify directly at the reach scale. This

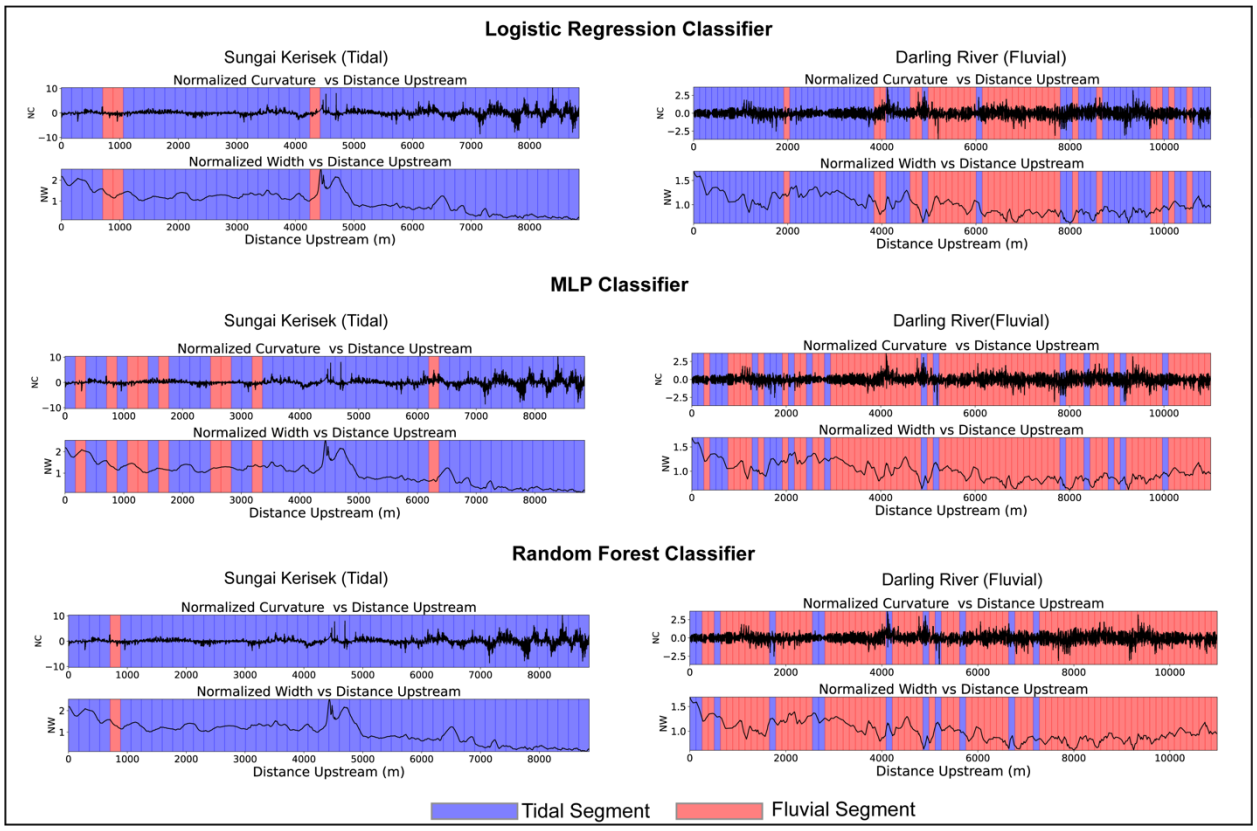

Figure 10: Segment-wise comparison of three classifiers for Sungai Kerisek (tidal) and Darling River (fluvial). Blue segments are tidal and red segments are fluvial. Normalized width (NW) and normalized curvature (NC) signals have been added to each.

approach requires the classification models to have accuracies at the segment scale that are well above 50%. In instances where a model is correct in more than 50% of segments, simple majority reach-scale classification thresholds can be applied. In this study the Random Forest (89-97%),MLP (82-95%), and Logistic Regression (64-90%) classifiers had segment-scale accuracies well over 50%. Interpretation of the spatial distribution of channel segment types for classified reaches should be handled with caution, especially when downstream hierarchies (i.e. fluvial segments cannot be downstream of tidal segments) exist. Channel segments with geometries similar to both tidal and fluvial channels may be misclassified, and the re-classification of downstream segments on this basis may be incorrect. In future work, use of convolutional neural networks and continuous wavelet transform representations of channel reaches may permit direct classification at the reach scale without the need for segmentation or even statistical representations of the channel geometry, while simultaneously preserving sub- to supra-meander scale structures.

2. Assessment of metric configurations

The best performing Random Forest classifier (trial 58) had a segment-scale accuracy of 95% and a reach-scale accuracy of 95% at the >50% threshold. The high segment-scale accuracy translated to high

reach-scale accuracy at the >50% and >66% thresholds but did not translate to equally high accuracy at the 75% threshold. This trial excluded 56 statistical variables derived from NC, NCxNW, NC' and, NCxNW', but did include those from NC/NW. Earlier trials (1-12) that include the 56 additional statistical variables had slightly higher segment-scale accuracies (96-97%), but poorer reach-scale accuracies. Trial 69, which had reach-scale accuracies identical to those of trial 58, did not include NC/NW but had lower segment scale accuracy (94%). This suggests that exclusion of normalized curvature-based variables positively influences the performance of classifiers evaluated at the reach scale, while having a minor negative influence on segment-scale accuracy.

Trial 58 included only principal channel metrics and statistical variables derived from normalized width (NW), normalized radius of curvature (NR), their convolutions (NRxNW), and their derivatives (NC/NW), and it excluded normalized curvature-based variables (NC), their convolutions (NCxNW), and derivatives. Because along-channel width and curvature can be used to reconstruct the planform geometry of a given channel reach (Vermeulen et al., 2016), it is not surprising that width and curvature emerge as two of the principal channel metrics. The Radius of curvature is the inverse of the absolute value of curvature, and unlike curvature, it has no directionality and is merely a representation of how curved a channel is at that point. The exclusion of normalized curvature-based variables from the most successful trial suggests that curvature may not be the best representation of local channel sharpness for the purposes of differentiation between channel types. This may be because the central tendency of normalized curvature values is near-zero for both channel types, a byproduct of its directionality that may inhibit differentiation. Similarly, curvature signals almost always oscillate between negative and positive values as channels change the direction of their bends. For example, segments that are right bending or left bending may have identical magnitude of curvature but with opposite signs due to the direction of the bend. This oscillation due to bend direction makes it difficult to identify relationships between channel sharpness and metrics that do not oscillate. However, this is not to say that curvature does not effectively record channel sharpness, which it certainly does, but instead that other representations of local channel sharpness such as radius of curvature may be better suited for differentiating between channel types and identifying relationships with other variables.

3. Feature importances and implications for differentiating channel types

Table 3 provides insight into the most important variables for classification according to the Random Forest classifier. The top 5 most important features are measures of the central tendency, minimum, and maximum of the normalized radius of curvature convolved with normalized width (NRxNW). The next 5 most important features are the midpoint, mean, and minimum of normalized width (NW) and ranges of the derivative of normalized width with respect to s (NW') and NRxNW. NRxNW is a representation of how normalized radius of curvature is modified by normalized width at any point along the channel. It can effectively highlight where the two variables are positively correlated. For example, points along a channel where the normalized width is high and normalized radius of curvature is high (i.e. low channel sharpness)

would have a high convolution value indicating there is a strong positive relationship between the two variables. The highest-ranking variable derived from normalized radius of curvature (NR) is the median NR, ranked 36th out of 88 with an overall importance of 0.0071. While normalized radius of curvature does contribute to the differentiation between channel types, its low importance relative to NW or NRxNW derived variables suggests it does not play a critical role in differentiating between channels. These rankings do indicate that the relationship between normalized radius of curvature (channel bend sharpness) and normalized channel width is more important for classification than normalized radius of curvature. In other words, the effect that local channel width at any point along the channel has on the sharpness of bends in the channel is more diagnostic than the actual sharpness of the bend at that point. Curvature is an important factor for the development and migration of channel bends, as bank erosion (e.g. active migration) has been shown to occur where curvature is the sharpest (Sylvester et al., 2019).

Table 3: Ranked Feature Importances for Trial 58

Rank	Variable Name	Importance
1	NRxNW Minimum	**0.1299**
2	NRxNW Median	**0.1062**
3	NRxNW Midpoint	**0.0845**
4	NRxNW Mean	**0.0682**
5	NRxNW Maximum	**0.0596**
6	NW Midpoint	**0.0224**
7	NW Mean	**0.0210**
8	NW Minimum	**0.0208**
9	NRxNW Range	**0.0207**
10	NW' Range	**0.0197**

Figure 11 shows the kernel density and cumulative density plots of normalized radius of curvature convolved with normalized width and normalized width, and plots of NRxNW and NW versus normalized distance upstream for tidal and fluvial channels. Kernel density plots of NRxNW show that tidal channels tend to have lower values of NRxNW (Fig. 11A), suggesting that tidal channels have configurations in which narrow channel widths co-occur with tighter bends (i.e. smaller radius of curvature). The distribution of NRxNW for fluvial channels is much broader than that of tidal channels, indicating a more complex or less direct relationship between local channel width and channel sharpness. This finding is consistent with results

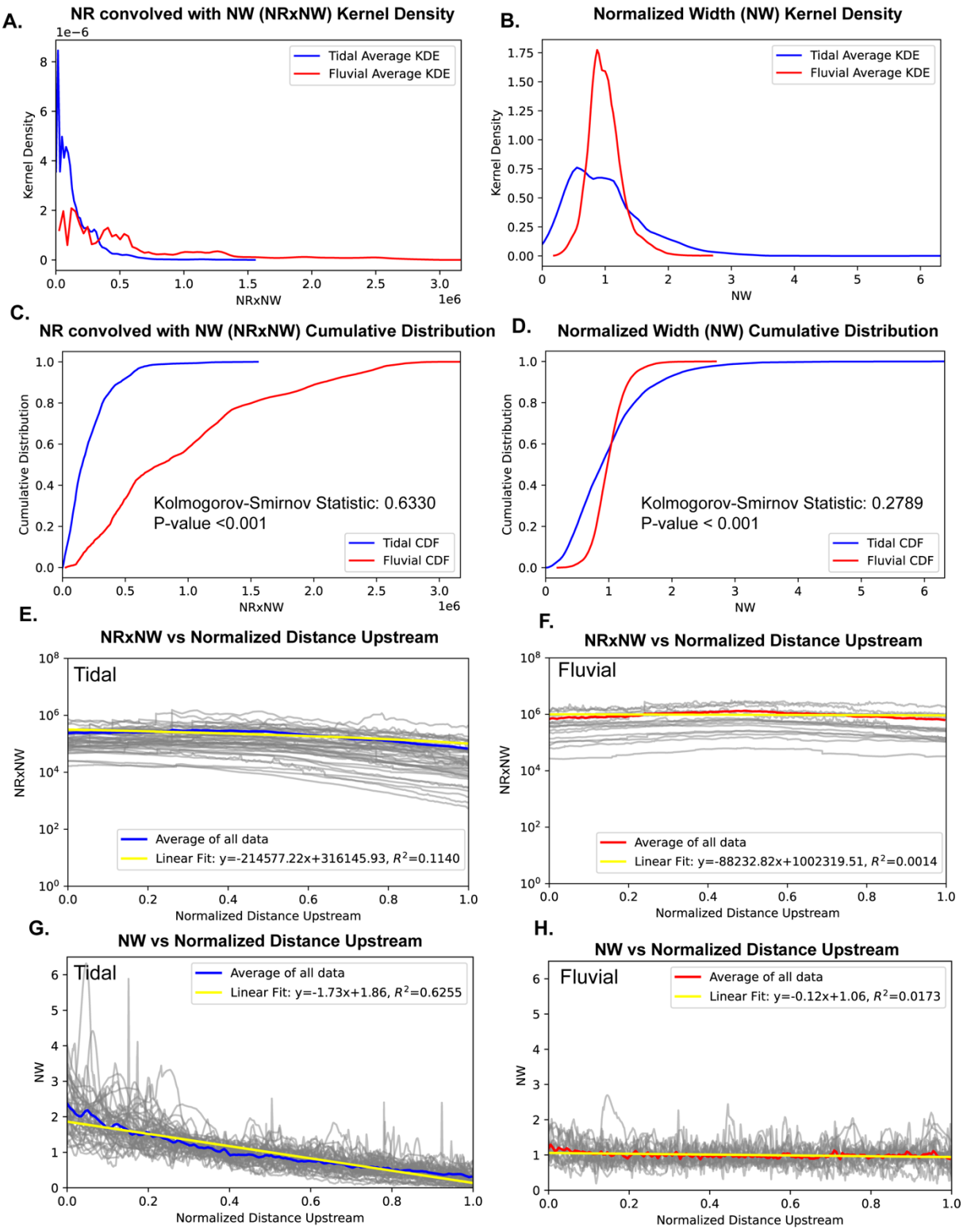

Figure 11: Statistical and along-channel plots of important principal along channel metrics, A,B: Kernel density plots showing distrubitons of NRxNW and NW for tidal and fluvial channels; C,D: Cumulative density functions NRxNW and NW for tidal and fluvial channels, Kolmogorov-Smirnov statistics indicate percent difference between functions in decimal form. Higher values indicate more separation. E,F: Plots of NRxNW vs normalized distance upstream for tidal and fluvial channels; G,H: Plots of NW vs normalized distance upstream for tidal and fluvial channels.

of Finotello *et al.* (2020), who found that fluvial channels have greater morphological complexity than tidal channels, and attributed the difference to fundamental differences in flow conditions between the two domains (Leopold et al., 1964). They segmented channel reaches into individual meanders, which allowed meander-specific metrics not included in our study to provide insight into morphological differences (Finotello *et al.,* 2020). The difference between morphological complexities of tidal and fluvial channels isresolvable both in meanders and smaller segments. Kernel density plots of NW (Fig. 11B) show that fluvial channels have a much higher density around normalized widths of 1, indicating that channel width for a fluvial reach does not vary significantly relative to its average, and rarely exceeds 2 times the average width. Tidal channels have normalized widths close to 1 in most instances, but the distribution is highly positively skewed relative to fluvial channels with normalized widths exceeding 6 times the average channel width. These pronounced differences result from normalization of local channel width by the average width of the channel at the reach scale and reflect the characteristic downstream increase in channel width observed in many tidal channels (Fagherazzi et al., 2004a; Lanzoni and D'Alpaos, 2015; Marani et al., 2002). Cumulative density plots and non-parametric Kolmogorov-Smirnov (K-S) tests of NRxNW and NW (Figs. 11C, D) quantify the differences in the distributions between channel types. Figure 11C shows a K-S statistic of 0.6330 with a p value of <0.001, indicating that fluvial and tidal distributions of NRxNW are statistically different at a significant level, and likely reflect different processes driving the relationship between normalized radius of curvature and normalized width. Figure 11D shows the CDF of normalized width and has a K-S statistic of 0.2789 at a p-value of <0.001. This indicates that the distributions of normalized width for tidal and fluvial channels are significantly different, although to a lesser magnitude than NRxNW. The distributions and significant differences in NRxNW and NW between channel types are consistent with high feature importance rankings of variables derived from these metrics.

Along-channel patterns in NRxNW for tidal channels (Fig. 11E) shows a gradual decrease in NRxNW in the upstream direction, suggesting that high radii of curvature are associated with higher widths at the mouths, and lower radii of curvature are associated with narrower widths in the upstream portions of reaches. This contrasts with the along-channel pattern of NRxNW for fluvial channels, which display relatively little change in the NRxNW in the upstream direction (Fig. 11F). In addition, tidal channels display a quasi-exponential decrease in channel width in the upstream direction (Fig. 11G), a pattern recognized in other prior studies (Fagherazzi et al., 2004a; Lanzoni and D'Alpaos, 2015; Marani et al., 2002). In contrast, the along-channel distribution of normalized width for fluvial channels shows relatively consistent channel widths (Fig. 11H), with values fluctuating irregularly around 1. This pattern likely results in more complex or less direct relationships between normalized width and normalized radius of curvature. While upstream narrowing of tidal channels has been recognized in prior studies (Fagherazzi et al., 2004; Lanzoni and D'Alpaos, 2015; Marani et al., 2002), this study is the first to incorporate this pattern into machine-learning and statistical analysis via reach-scale normalization of segments. Additionally, this study is the first study to quantify the

morphological relationship between normalized width and normalized radius of curvature via convolution of the two along-channel signals, which we use to classify channels using machine-learning algorithms.

4. Implications for interpreting relict channels and mixed-energy settings

While recognition of channel type is typically straightforward in modern settings, methods developed here offer promising potential to study ancient, relict channels preserved on inactive low-relief surfaces. Because tidal channels generally form within 1-5 meters of mean sea level, recognition of tidal channels on relict surfaces can provide useful constraints on changes in relative sea level and vertical crustal motions. Conversely, fluvial channels provide no information about relative sea-level change or uplift rates. Low-relief geomorphic surfaces with preserved channel planforms are known from uplifting coastal landscapes in active tectonics settings around the world, including: (1) rift-flank uplifts adjacent to extensional and transtensional plate boundaries (e.g., Red Sea and Gulf of Suez (Morag et al., 2019); Baja California, Mexico (Ortlieb, 1991)); (2) young uplifts in zones of active continental collision (e.g., Persian Gulf of southwest Iran (Berberian, 1995); Ganges-Brahmaputra Delta in southern Bangladesh (Kuehl et al., 2005)); and (3) forearc regions undergoing uplift above active subduction zones (e.g., southwest Japan, North Island of New Zealand, Cascadia of western North America, and Chilean margin of South America (Menant et al., 2020)). These regions offer the potential for study of preserved inactive low-relief landscapes to identify and use relict tidal channels to gain improved understanding of uplift histories.

The channel reaches used in this study were either completely fluvial or completely tidal. This choice was made intentionally, to have as little overlap in channel origin as possible for the purposes of machine learning. However, mixed tidal and fluvial energy settings are are commonly observed in estuaries. While the methodology developed in this paper can be applied to future studies of channels in mixed tidal-fluvial settings, important factors should be considered. For example, misclassification of channel segments is likely to occur at higher rates in mixed-energy settings, because the juxtaposition of contrasting processes may produce intermediate morphologies unfamiliar to the trained classifier. Segmentation in this methodology was implemented to preserve local channel geometries while also allowing for segments to be analyzed in the context of the channel type, and thus misclassifications can place tidal segments in purely fluvial channels and vice versa. This challenge can potentially be addressed through use of geographical markers to identify tidally-dominant versus fluvially-dominant sections in estuary systems. For example, a decrease in abundance of tidally-classified segments upstream of the furthest inland extent of modern tides would suggest that our methodology can be applied to a mixed-energy setting. It may also be possible to implement a third classification category that represents mixed energy or undifferentiable segments.

CONCLUSIONS

We present a machine learning-based classification method that uses reach-normalized data to classify channels as either tidal or fluvial. Through training multiple classifiers on a global dataset of tidal and fluvial channels we find: (1) Linear Discriminant Analysis is not sufficient for classification; (2) the Random Forest classifier demonstrated 100 % accuracy at classifying "unknown" channel reaches at the >50% classification threshold, indicating that this classification method is robust and reliable; and (3) the convolution of normalized radius of curvature with normalized width (NRxNW) and normalized width (NW) are more successful for differentiating tidal channels using this approach than the magnitude of local curvature.

This methodology offers the potential to identify relict tidal channels on inactive low-relief surfaces and constrain uplift histories in a wide range of tectonic and physiographic settings. It may also be possible to analyze channel planforms in mixed-energy settings using this approach, although care must be taken when interpreting the spatial arrangement of classified segments. Future work could use wavelet representations of channel morphologies and train convolutional neural networks to classify channels directly at the reach scale while retaining sub- and supra-meander structures.

ACKNOWLEDGMENTS

This work was funded by National Science Foundation grant EAR-1925560 to Dorsey

REFERENCES CITED: In ESPL format

Berberian M. 1995. Master "blind" thrust faults hidden under the Zagros folds: active basement tectonics and surface morphotectonics. Tectonophysics **241** : 193–224. DOI: 10.1016/0040-1951(94)00185-C [online] Available from: https://linkinghub.elsevier.com/retrieve/pii/004019519400185C

Breiman L. 2001. Random forests. Machine learning **45** : 5–32.

Bressan TS, Kehl de Souza M, Girelli TJ, Junior FC. 2020. Evaluation of machine learning methods for lithology classification using geophysical data. Computers & Geosciences **139** : 104475. DOI: 10.1016/J.CAGEO.2020.104475

Corbi F, Sandri L, Bedford J, Funiciello F, Brizzi S, Rosenau M, Lallemand S. 2019. Machine Learning Can Predict the Timing and Size of Analog Earthquakes. Geophysical Research Letters **46** : 1303–1311. DOI: 10.1029/2018GL081251 [online] Available from: https://onlinelibrary.wiley.com/doi/full/10.1029/2018GL081251 (Accessed 13 March 2024)

Cracknell MJ, Reading AM. 2014. Geological mapping using remote sensing data: A comparison of five machine learning algorithms, their response to variations in the spatial distribution of training data and the use of explicit spatial information. Computers & Geosciences **63** : 22–33. DOI: 10.1016/J.CAGEO.2013.10.008

Das P, Pandey V. 2019. Use of logistic regression in land-cover classification with moderate-resolution multispectral data. Journal of the Indian Society of Remote Sensing **47** : 1443–1454. [online] Available from: Use of logistic regression in land-cover classification with moderate-resolution multispectral data

Evans DL, Farr TG, Ford JP, Thompson TW, Werner CL. 1986. Multipolarization Radar Images for Geologic Mapping and Vegetation Discrimination. IEEE Transactions on Geoscience and Remote Sensing **GE-24** : 246–257. DOI: 10.1109/TGRS.1986.289644

Fagherazzi S, Gabet EJ, Furbish DJ. 2004. The effect of bidirectional flow on tidal channel planforms. Earth Surface Processes and Landforms **29** : 295–309. DOI: 10.1002/esp.1016

El Fels AEA, El Ghorfi M. 2022. Using remote sensing data for geological mapping in semi-arid environment: a machine learning approach. Earth Science Informatics **15** : 485–496. DOI: 10.1007/S12145-021-00744-W/METRICS [online] Available from: https://link.springer.com/article/10.1007/s12145-021-00744-w (Accessed 5 March 2024)

Finotello A, D'Alpaos A, Bogoni M, Ghinassi M, Lanzoni S. 2020. Remotely-sensed planform morphologies reveal fluvial and tidal nature of meandering channels. Scientific Reports 2020 10:1 **10** : 1–13. DOI: 10.1038/s41598-019-56992-w [online] Available from: https://www.nature.com/articles/s41598-019-56992-w

Finotello A, Ielpi A, Lapôtre MGA, Lazarus ED, Ghinassi M, Carniello L, Favaro S, Tognin D, D'Alpaos A. 2024. Vegetation enhances curvature-driven dynamics in meandering rivers. Nature Communications **15** : 1968.

Finotello A, Lanzoni S, Ghinassi M, Marani M, Rinaldo A, D'Alpaos A. 2018. Field migration rates of tidal meanders recapitulate fluvial morphodynamics. Proceedings of the National Academy of Sciences **115** : 1463–1468. DOI: 10.1073/pnas.1711330115

Gao C et al. 2024. Morphometry of Tidal Meander Cutoffs Indicates Similarity to Fluvial Morphodynamics. Geophysical Research Letters **51** : e2023GL105893. DOI: 10.1029/2023GL105893 [online] Available from: https://onlinelibrary.wiley.com/doi/full/10.1029/2023GL105893

Gardner K, Dorsey RJ. 2021. Mixed carbonate–siliciclastic sedimentation at the margin of a late Miocene tidal strait, lower Colorado River Valley, south-western USA. Betzler C (ed). Sedimentology : sed.12834. DOI: 10.1111/sed.12834

Golly A, Turowski JM. 2017. Deriving principal channel metrics from bank and long-profile geometry with the R package cmgo. Earth Surface Dynamics **5** : 557–570. DOI: 10.5194/esurf-5-557-2017 [online] Available from: https://esurf.copernicus.org/articles/5/557/2017/

Hinton GE. 1990. CONNECTIONIST LEARNING PROCEDURES. In Machine Learning , Kodratoff Y and Michalski RS (eds). Elsevier: San Francisco (CA); 555–610. [online] Available from: https://linkinghub.elsevier.com/retrieve/pii/B9780080510552500298

Horton RE. 1945. Erosional development of streams and their drainage basins: hydrophysical approach to quantitative morphology. Geological Society of America Bulletin **56** : 275–370. DOI: https://doi.org/10.1130/0016-7606(1945)56[275:EDOSAT]2.0.CO;2

Hughes ZJ. 2012. Tidal Channels on Tidal Flats and Marshes. In Principles of Tidal Sedimentology , Davis RA and Dalrymple RW (eds). Springer Netherlands: Dordrecht; 35–55.

Keshtkar H, Voigt W, Alizadeh E. 2017. Land-cover classification and analysis of change using machine-learning classifiers and multi-temporal remote sensing imagery. Arabian Journal of Geosciences **10** : 1–15.

Kingma DP, Ba J. 2014. Adam: A method for stochastic optimization. arXiv preprint arXiv:1412.6980

Kong JA, Swartz AA, Yueh HA, Novak LM, Shin RT. 1988. Identification of terrain cover using the optimum polarimetric classifier. Journal of Electromagnetic Waves and Applications **2** : 171–194. DOI: 10.1163/156939387X00324

Kuehl SA, Allison MA, Goodbred SL, Kudrass H. 2005. The ganges-brahmaputra delta

Kvale EP, Cutright J, BIlodeau D, Archer A, Johnson HR, Pickett B. 1995. Analysis of modern tides and implications for ancient tidalites. Continental Shelf Research **15** DOI: 10.1016/0278-4343(95)00001-H

Lanzoni S, D'Alpaos A. 2015. On funneling of tidal channels. Journal of Geophysical Research: Earth Surface **120** : 433–452. DOI: 10.1002/2014jf003203

Lanzoni S, Seminara G. 1998. On tide propagation in convergent estuaries. Journal of Geophysical Research: Oceans **103** : 30793–30812. DOI: 10.1029/1998JC900015 [online] Available from: https://onlinelibrary.wiley.com/doi/full/10.1029/1998JC900015 (Accessed 13 March 2024)

Lee JS, Grunes MR, Kwok R. 1994. Classification of multi-look polarimetric SAR imagery based on complex Wishart distribution. International Journal of Remote Sensing **15** : 2299–2311. DOI: 10.1080/01431169408954244

Leopold LB, Wolman MG. 1957. River channel patterns: braided, meandering, and straight . US Government Printing Office: Washington, D.C.

Leopold LB, Wolman MG, Miller JP. 1964b. Fluvial processes in geomorphology . Dover Publications, Inc.: New York, NY

Lunine JI, Lorenz RD. 2009. Rivers, Lakes, Dunes, and Rain: Crustal Processes in Titan's Methane Cycle. Annual Review of Earth and Planetary Sciences **37** : 299–320. DOI: 10.1146/annurev.earth.031208.100142

Lutscher F, McCauley E, Lewis MA. 2007. Spatial patterns and coexistence mechanisms in systems with unidirectional flow. Theoretical Population Biology **71** : 267–277. DOI: 10.1016/j.tpb.2006.11.006

Marani M et al. 2003. On the drainage density of tidal networks. Water Resources Research **39** : 1040. DOI: 10.1029/2001WR001051 [online] Available from: https://onlinelibrary.wiley.com/doi/full/10.1029/2001WR001051 (Accessed 11 March 2024)

Marani M, Lanzoni S, Zandolin D, Seminara G, Rinaldo A. 2002. Tidal meanders. Water Resources Research **38** : 7–14. DOI: 10.1029/2001wr000404

McCullagh P. 2019. Generalized linear models . Routledge

Menant A, Angiboust S, Gerya T, Lacassin R, Simoes M, Grandin R. 2020. Transient stripping of subducting slabs controls periodic forearc uplift. Nature communications **11** : 1823.

Morag N, Haviv I, Eyal M, Kohn BP, Feinstein S. 2019. Early flank uplift along the Suez Rift: Implications for the role of mantle plumes and the onset of the Dead Sea Transform. Earth and Planetary Science Letters **516** : 56–65.

Murti MA, Junior R, Ahmed AN, Elshafie A. 2022. Earthquake multi-classification detection based velocity and displacement data filtering using machine learning algorithms. Scientific Reports 2022 12:1 **12** : 1–12.

DOI: 10.1038/s41598-022-25098-1 [online] Available from: https://www.nature.com/articles/s41598-022-25098-1 (Accessed 13 March 2024)

Novakowski KI, Torres R, Gardner LR, Voulgaris G. 2004. Geomorphic analysis of tidal creek networks. Water Resources Research **40** DOI: 10.1029/2003WR002722

Ortlieb L. 1991. Quaternary shorelines along the northeastern Gulf of California, geochronological data and neotectonic implications. Geological Society of America. Special Paper **254** : 95–120.

Parikh H, Patel S, Patel V. 2020. Classification of SAR and PolSAR images using deep learning: a review. International Journal of Image and Data Fusion **11** : 1–32. DOI: 10.1080/19479832.2019.1655489

Pedregosa F, Varoquaux G, Gramfort A, Michel V, Thirion B, Grisel O, Blondel M, Prettenhofer P, Weiss R, Dubourg V. 2011. Scikit-learn: Machine learning in Python. the Journal of machine Learning research **12** : 2825–2830.

Rinaldo A, Fagherazzi S, Lanzoni S, Marani M, Dietrich WE. 1999. Tidal networks: 2. Watershed delineation and comparative network morphology. Water Resources Research **35** : 3905–3917. DOI: 10.1029/1999WR900237 [online] Available from: http://doi.wiley.com/10.1029/1999WR900237

Sylvester Z, Durkin P, Covault JA. 2019. High curvatures drive river meandering. Geology **47** : 263–266.

Vermeulen B, Hoitink AJF, Zolezzi G, Abad JD, Aalto R. 2016a. Multiscale structure of meanders. Geophysical Research Letters **43** : 3288–3297. DOI: 10.1002/2016GL068238

Wang W, Xue C, Zhao J, Yuan C, Tang J. 2024. Machine learning-based field geological mapping: A new exploration of geological survey data acquisition strategy. Ore Geology Reviews **166** : 105959. DOI: 10.1016/J.OREGEOREV.2024.105959

Supplementary File S1: Tab-Delimited Text of Reach-Scale and Segment-Scale Accuracies for the three ML Classifiers

Rows 1-9: Reach scale accuracies for each classifier at each reach-scale classification threshold; Rows 10-12 Segment-scale accuracy for each ML classifier. Each data row represents an individual trial run from 1-69 in order.

MLP_Reach_>50% MLP_Reach_>66% MLP_Reach_>75%
RandomForest_Reach_>50% RandomForest_Reach_>66%
RandomForest_Reach_>75% LogisticRegression_Reach_>50%
LogisticRegression_Reach__>66% LogisticRegression_Reach_>75%
MLP_Segment_Testing_Accuracy   RandomForest_Segment_Testing_Accuracy
        LogisticRegression_Segment_Testing_Accuracy

100	85	70	95	85	75	85	85	75
	0.920838184		0.966239814		0.884749709			
95	80	70	95	85	70	75	60	50
	0.915017462		0.966239814		0.697322468			
100	85	70	95	85	70	80	75	70
	0.939464494		0.962747381		0.891734575			
100	90	65	95	85	75	85	85	75
	0.915017462		0.969732247		0.878928987			
95	85	75	95	85	80	75	60	50
	0.902211874		0.969732247		0.697322468			
95	75	70	95	85	75	85	75	70
	0.949941793		0.970896391		0.895227008			
95	85	65	95	90	70	85	80	80
	0.913853318		0.965075669		0.884749709			
95	85	70	95	90	75	85	60	55
	0.908032596		0.962747381		0.70314319			
90	80	70	95	90	75	80	75	70
	0.94644936		0.962747381		0.889406286			
100	85	75	95	90	75	85	80	75
	0.92782305		0.966239814		0.881257276			
90	80	80	95	85	75	85	60	55
	0.902211874		0.963911525		0.70314319			
100	75	70	95	90	70	85	75	70
	0.923166473		0.965075669		0.894062864			
85	80	60	85	75	70	75	75	65
	0.857974389		0.90919674		0.87427241			
85	60	60	85	75	70	70	55	25
	0.860302678		0.912689173		0.663562282			
80	75	60	85	75	75	80	65	60
	0.892898719		0.911525029		0.873108265			
95	65	60	85	75	70	75	75	65
	0.842840512		0.912689173		0.868451688			
85	60	60	85	80	70	70	50	40
	0.875436554		0.913853318		0.715948778			
75	75	65	85	80	70	80	70	60
	0.892898719		0.913853318		0.875436554			

95	70	55	85	80	70	75	65
	0.852153667		0.908032596		0.867287544		
90	75	60	85	80	70	70	60	40
	0.846332945		0.90919674		0.721769499		
90	70	60	85	80	70	80	70	60
	0.863795111		0.904540163		0.870779977		
90	80	50	85	80	80	85	85	70
	0.82887078		0.923166473		0.806752037		
90	80	65	85	80	75	70	55	55
	0.82887078		0.920838184		0.637951106		
95	70	45	85	80	75	70	65	60
	0.862630966		0.926658906		0.782305006		
90	75	50	85	80	80	85	85	70
	0.835855646		0.916181607		0.806752037		
85	80	75	85	80	75	70	55	55
	0.8556461		0.913853318		0.637951106		
85	75	70	85	80	75	70	65	60
	0.891734575		0.915017462		0.782305006		
85	75	60	90	80	70	85	80	70
	0.82887078		0.892898719		0.811408615		
85	75	65	90	80	70	80	70	60
	0.820721769		0.892898719		0.647264261		
80	80	75	90	80	70	75	65	60
	0.854481956		0.894062864		0.769499418		
85	75	70	90	80	65	85	80	70
	0.830034924		0.898719441		0.811408615		
85	65	45	90	80	65	80	70	60
	0.816065192		0.902211874		0.647264261		
90	80	70	90	80	65	75	65	60
	0.870779977		0.899883586		0.768335274		
90	70	60	100	75	65	80	75	75
	0.895227008		0.948777648		0.883585565		
100	70	60	100	75	65	80	50	50
	0.899883586		0.94644936		0.701979045		
95	80	70	100	75	65	85	75	65
	0.923166473		0.948777648		0.884749709		
95	75	60	100	80	65	80	75	75
	0.889406286		0.941792782		0.883585565		
100	70	55	100	75	70	80	50	50
	0.902211874		0.939464494		0.701979045		
100	80	70	100	75	70	85	75	65
	0.925494761		0.941792782		0.884749709		
90	65	60	90	85	70	80	75	75
	0.895227008		0.941792782		0.884749709		
90	75	65	95	85	70	85	60	50
	0.910360885		0.945285215		0.772991851		
95	75	65	90	85	75	85	75	75
	0.903376019		0.942956927		0.88242142		
90	70	60	90	80	65	80	75	75
	0.890570431		0.945285215		0.884749709		

90	75	65	95	85	70	85	60	50
	0.910360885		0.945285215		0.772991851			
90	90	75	95	85	70	85	75	75
	0.906868452		0.944121071		0.88242142			
95	80	65	85	80	70	95	85	75
	0.841676368		0.91967404		0.834691502			
85	75	65	85	80	70	70	65	55
	0.864959255		0.917345751		0.650756694			
85	70	70	85	80	70	80	75	65
	0.871944121		0.913853318		0.75669383			
90	70	60	85	80	75	95	85	75
	0.868451688		0.913853318		0.824214203			
85	75	70	85	80	75	70	60	55
	0.866123399		0.918509895		0.648428405			
85	80	75	85	80	75	85	65	60
	0.881257276		0.918509895		0.762514552			
90	75	65	85	75	70	95	80	75
	0.83701979		0.908032596		0.817229336			
90	75	65	85	75	70	70	70	60
	0.868451688		0.903376019		0.67636787			
85	75	75	85	75	70	90	65	65
	0.902211874		0.906868452		0.747380675			
90	85	55	85	85	70	95	80	70
	0.849825378		0.911525029		0.827706636			
80	70	65	85	85	70	70	70	60
	0.8556461		0.911525029		0.679860303			
85	75	70	85	85	75	80	70	65
	0.892898719		0.911525029		0.747380675			
95	75	70	100	95	75	80	80	80
	0.892898719		0.945285215		0.889406286			
100	75	65	100	90	70	80	50	50
	0.885913853		0.940628638		0.699650757			
95	85	70	100	95	70	85	70	60
	0.920838184		0.942956927		0.892898719			
100	80	65	100	90	65	80	80	80
	0.898719441		0.942956927		0.889406286			
100	85	70	100	90	65	80	50	50
	0.88242142		0.945285215		0.699650757			
95	90	80	100	90	65	85	70	60
	0.928987194		0.944121071		0.892898719			
100	75	70	100	90	70	80	80	75
	0.894062864		0.940628638		0.878928987			
95	80	65	100	85	75	80	60	60
	0.883585565		0.940628638		0.679860303			
95	90	75	100	85	75	85	75	65
	0.934807916		0.939464494		0.884749709			
95	75	70	100	90	75	80	80	75
	0.905704307		0.942956927		0.878928987			
95	85	75	100	90	75	80	60	60
	0.904540163		0.944121071		0.679860303			

95 90 85 100 95 75 85 75 65

0.934807916 0.942956927 0.884749709

Supplementary File S2: Ranked Feature Importances given by the Random Forest classifier from the trial with the highest reach-scale accuracy (Trial 58).

ROC = Radius of Curvature, NC = Normalized Curvature, NW = Normalized Width

1. Normalized ROC Conv Normalized Width Min: 0.1299
2. Normalized ROC Conv Normalized Width Median: 0.1062
3. Normalized ROC Conv Normalized Width Midpoint: 0.0845
4. Normalized ROC Conv Normalized Width Mean: 0.0682
5. Normalized ROC Conv Normalized Width Max: 0.0596
6. Normalized Width Midpoint: 0.0224
7. Normalized Width Mean: 0.0210
8. Normalized Width Min: 0.0208
9. Normalized ROC Conv Normalized Width Range: 0.0207
10. D Normalized Width Ds Range: 0.0197
11. Normalized Width Max: 0.0187
12. NC/NW Variance: 0.0148
13. D Normalized Width Ds Variance: 0.0145
14. Normalized Width Median: 0.0144
15. D Normalized ROC Conv Normalized Width Ds Mean Abs Dev: 0.0139
16. D Normalized Width Ds Min: 0.0137
17. D Normalized Width Ds Std Dev: 0.0136
18. D Normalized ROC Conv Normalized Width Ds Std Dev: 0.0123
19. D Normalized ROC Conv Normalized Width Ds Iqr: 0.0118
20. D Normalized Width Ds Mean Abs Dev: 0.0117
21. D Normalized ROC Conv Normalized Width Ds Median: 0.0103
22. Normalized ROC Conv Normalized Width Variance: 0.0102
23. Normalized ROC Conv Normalized Width Std Dev: 0.0099
24. NC/NW Iqr: 0.0097
25. NC/NW Mean Abs Dev: 0.0095
26. D Normalized ROC Conv Normalized Width Ds Mean: 0.0091
27. D Normalized ROC Conv Normalized Width Ds Min: 0.0090
28. NC/NW Max: 0.0087
29. D Normalized Radius Of Curvature Ds Iqr: 0.0084
30. D Normalized ROC Conv Normalized Width Ds Variance: 0.0081
31. D Normalized ROC Conv Normalized Width Ds Mode: 0.0078
32. Normalized ROC Conv Normalized Width Mean Abs Dev: 0.0075
33. D Normalized ROC Conv Normalized Width Ds Kurtosis: 0.0073
34. Normalized ROC Conv Normalized Width Iqr: 0.0072
35. D Normalized ROC Conv Normalized Width Ds Range: 0.0071
36. Normalized Radius Of Curvature Median: 0.0071
37. NC/NW Std Dev: 0.0069
38. NC/NW Min: 0.0063
39. NC/NW Mode: 0.0062
40. D Normalized ROC Conv Normalized Width Ds Max: 0.0060
41. Normalized Radius Of Curvature Mode: 0.0057
42. D Normalized Width Ds Iqr: 0.0057
43. D Normalized Radius Of Curvature Ds Mean Abs Dev: 0.0054
44. D Normalized ROC Conv Normalized Width Ds Skewness: 0.0048

45. Normalized Radius Of Curvature Min: 0.0046
46. NC/NW Range: 0.0045
47. D Normalized Width Ds Max: 0.0043
48. D Normalized Width Ds Median: 0.0042
49. Normalized Radius Of Curvature Iqr: 0.0039
50. D Normalized ROC Conv Normalized Width Ds Midpoint: 0.0036
51. NC/NW Median: 0.0036
52. Normalized Width Range: 0.0035
53. D Normalized Width Ds Midpoint: 0.0034
54. NC/NW Skewness: 0.0032
55. D Normalized Radius Of Curvature Ds Std Dev: 0.0032
56. Normalized Width Skewness: 0.0032
57. NC/NW Mean: 0.0031
58. D Normalized Radius Of Curvature Ds Range: 0.0031
59. Normalized Width Mean Abs Dev: 0.0031
60. Normalized Radius Of Curvature Mean: 0.0030
61. D Normalized Radius Of Curvature Ds Median: 0.0030
62. NC/NW Kurtosis: 0.0030
63. D Normalized Radius Of Curvature Ds Min: 0.0030
64. Normalized Width Iqr: 0.0030
65. Normalized Width Variance: 0.0029
66. D Normalized Radius Of Curvature Ds Mean: 0.0028
67. Normalized Width Std Dev: 0.0027
68. D Normalized Width Ds Mean: 0.0027
69. D Normalized Width Ds Skewness: 0.0025
70. D Normalized Radius Of Curvature Ds Max: 0.0025
71. Normalized Radius Of Curvature Mean Abs Dev: 0.0025
72. NC/NW Midpoint: 0.0025
73. Normalized ROC Conv Normalized Width Skewness: 0.0024
74. D Normalized Radius Of Curvature Ds Skewness: 0.0024
75. Normalized Radius Of Curvature Skewness: 0.0024
76. D Normalized Radius Of Curvature Ds Mode: 0.0023
77. D Normalized Width Ds Kurtosis: 0.0023
78. D Normalized Radius Of Curvature Ds Midpoint: 0.0022
79. Normalized ROC Conv Normalized Width Kurtosis: 0.0022
80. Normalized Width Kurtosis: 0.0021
81. Normalized Radius Of Curvature Range: 0.0020
82. Normalized Radius Of Curvature Kurtosis: 0.0019
83. Normalized Radius Of Curvature Max: 0.0019
84. Normalized Radius Of Curvature Variance: 0.0019
85. Normalized Radius Of Curvature Std Dev: 0.0019
86. D Normalized Radius Of Curvature Ds Kurtosis: 0.0019
87. Normalized Radius Of Curvature Midpoint: 0.0017
88. D Normalized Radius Of Curvature Ds Varian